

# Multiscale modeling of compaction bands in saturated high-porosity sandstones



Huanran Wu<sup>a</sup>, Jidong Zhao<sup>a,b,\*</sup>, Ning Guo<sup>c</sup>

<sup>a</sup> Department of Civil and Environmental Engineering, Hong Kong University of Science and Technology, Clearwater Bay, Kowloon, Hong Kong

<sup>b</sup> Hong Kong University of Science and Technology Shenzhen Research Institute, Shenzhen, China

<sup>c</sup> Research Center of Coastal and Urban Geotechnical Engineering, College of Civil Engineering and Architecture, Zhejiang University, 866 Yuhangtang Rd, Hangzhou, Zhejiang 310058, China

## ARTICLE INFO

### Keywords:

Compaction band  
Band pattern transition  
Saturated high-porosity sandstone  
Hydro-mechanical multiscale modeling  
Excess pore pressure

## ABSTRACT

We propose a hierarchical multiscale modeling approach to simulate the hydro-mechanical coupling behavior in saturated high-porosity sandstone, with a particular focus on the occurrence and transition of compaction bands. In this multiscale approach, we use the finite element method (FEM) to solve the global boundary value problem for a sandstone, and the discrete element method (DEM) to solve the local representative volume elements (RVEs) embedded at the Gauss integration points of the FE mesh to provide the effective material constitutive responses required for FEM. The global governing equations for a coupled hydro-mechanical problem are solved with the standard  $u-p$  formulation, where the total stress is decomposed into the pore pressure and the effective stress which is directly derivable from the DEM solution of the RVEs, according to the seminal Terzaghi's effective stress principle. By choosing proper RVEs to represent the typical microstructure of high-porosity sandstone, we perform both drained and undrained simulations on saturated sandstone specimens to examine localized compactive failures developed therein. We identify that both mean effective stress and porosity control critically the initiation and development of failure modes in sandstone. Under undrained shear, our simulations show that a sandstone specimen may first develop a compaction band followed by a gradual transition to a shear-enhanced compaction band and even shear band, with the build-up of excessive pore pressure and hence drop of mean effective stress. In the specimen, regions experiencing localized volumetric contraction show relatively higher pore pressure than other regions and act as the source of flux flow. The Darcy flux peaks during the formation of compaction band and decreases gradually in the following stages. To distinguish the different failure stages with distinct physical attributes, the ratio of deviatoric strain to volumetric strain is adopted as a useful indicator signifying the underlying microstructural mechanisms for different deformation bands. This study signifies the importance of considering pore pressure and mean effective stress in fluid-involved engineering operations, e.g. aquifer management, hydrocarbon extraction and CO<sub>2</sub> geological sequestration.

## 1. Introduction

Deformation bands, occurring as narrow tabular zones with localized strain and small offsets in porous rocks (Fossen et al., 2017), are widely observed in high-porosity sandstones in field observations, laboratory experiments and numerical simulations. Among different deformation bands, the compaction band with pure compaction deformation but little or no shear draws special attentions since its field observations (Mollema and Antonellini, 1996; Aydin and Ahmadov, 2009). Porous rocks, especially high-porosity sandstones, are economically important worldwide, as they are common hosts for groundwater

or hydrocarbon reservoirs, CO<sub>2</sub> storage and hazardous waste disposal (Holcomb et al., 2007). Their mechanical behaviors, especially their intricate interactions with the presence of pore fluids, are of great interest to the geomechanics and geotechnics community. The occurrence of deformation bands in these porous rocks, in particular compaction bands, add further complexity to their material behavior and pose extraordinary challenges for relevant practical operations, e.g. aquifer management, hydrocarbon extraction, CO<sub>2</sub> geological sequestration, etc. There is yet a great knowledge gap towards an integrated understanding of the interplays among pore fluids, rock skeletons and the formation and presence of various deformation bands in these

\* Corresponding author at: Department of Civil and Environmental Engineering, Hong Kong University of Science and Technology, Clearwater Bay, Kowloon, Hong Kong.

E-mail address: [jzhao@ust.hk](mailto:jzhao@ust.hk) (J. Zhao).

<https://doi.org/10.1016/j.enggeo.2019.105282>

Received 31 May 2019; Received in revised form 30 July 2019; Accepted 31 August 2019

Available online 04 September 2019

0013-7952/ © 2019 Elsevier B.V. All rights reserved.

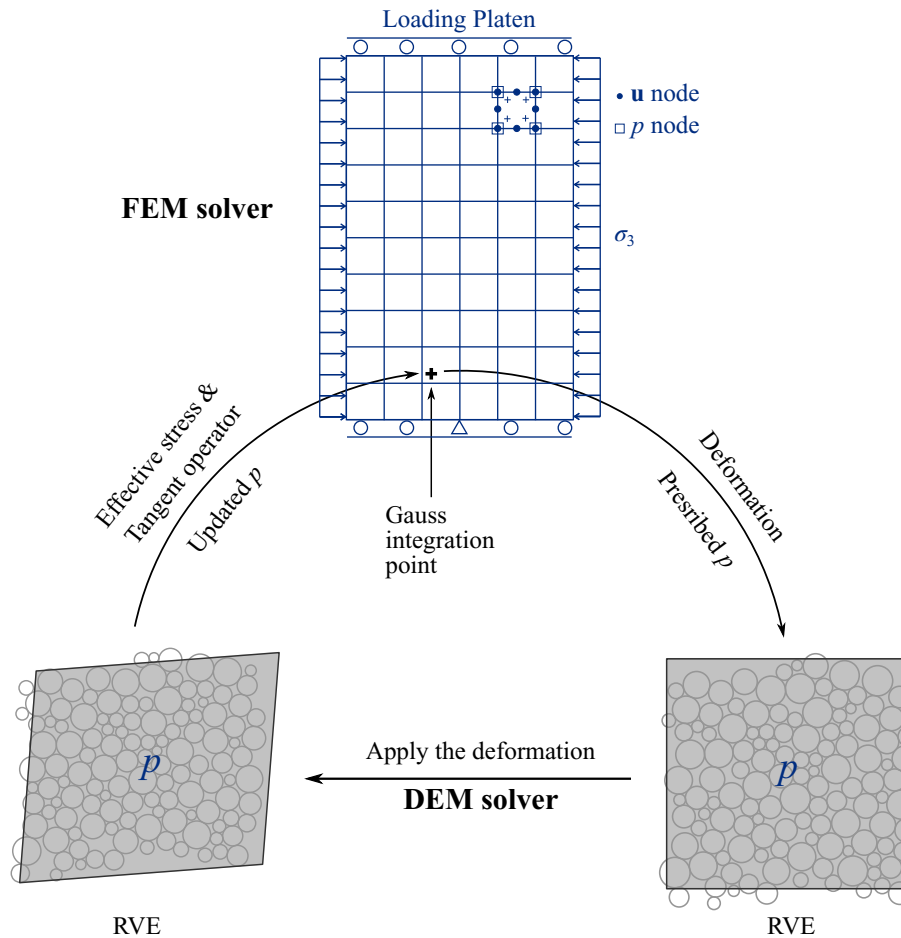


Fig. 1. Illustration of the coupled FEM/DEM multiscale scheme for hydro-mechanical modeling of saturated sandstone.

sandstones. Most critically, there are no effective predictive tools available for a thorough and rigorous appraisal of this important subject.

Indeed, the effect of pore fluid in porous granular media has long been recognized in civil and petroleum engineering since the pioneering work on consolidation and effective stress by Biot (1941) and Terzaghi (1943). Based on the effective stress principle by Terzaghi (1943), the coupled effects of pore pressure and mechanical responses of saturated soils have been investigated numerically based on continuum mechanics and mixture theory by Zienkiewicz and Chan (1989) following a  $\mathbf{u}$ - $p$  formulation ( $\mathbf{u}$ : the displacement of solid phase;  $p$ : the pore pressure) (see also Andrade and Borja, 2007). Some recent micromechanics-based attempts have been made to solve the solid phase with discrete element method (DEM) and the fluid phase with computational fluid dynamics (CFD) or lattice Boltzmann method (LBM) (Zhao and Shan, 2013; Sun et al., 2013). The influence of pore fluids on the elastic properties and failure behaviors of rocks have been investigated in laboratory experiments (Chang and Haimson, 2007; Wasantha and Ranjith, 2014; Wasantha et al., 2016; Zhang et al., 2019).

The occurrence of various deformation bands in porous rocks and other geomaterials has been well documented and investigated in relation with geological failures and natural hazards (e.g., landslides). There have been extensive experimental studies on the occurrence of compaction bands and other localized deformation patterns under both dry and saturated drained conditions (Baud et al., 2004; Tembe et al., 2008). The inception and further evolution of compaction bands have been examined with both theoretical models and numerical simulations (Issen and Rudnicki, 2000; Das and Buscarnera, 2014). Some

micromechanics-based approaches, such as DEM and spring network model, have been adopted to reproduce compaction bands and to analyze their underlying mechanisms (Katsman et al., 2006; Liu et al., 2015). Specifically, the presence of deformation bands may reduce the permeability of the matrix up to several orders of magnitude and hence potentially impede the fluid flow (Baud et al., 2012; Kimura et al., 2018). The influence of deformation bands on the fluid flow has been examined through water imbibition tests and tomography technologies (Pons et al., 2011; Hall, 2013).

However, the effects of pore fluid pressure on failure patterns, in the context of hydro-mechanical coupling in a saturated sandstone, have been less investigated. Among the limited studies, Sulem and Ouffroukh (2006) conducted experiments on water-saturated sandstone samples and compared the different microstructures of shear band in drained and undrained conditions. Ougier-Simonin and Zhu (2013) observed the failure patterns in porous sandstones changing from stable sliding faults to unstable slips due to the presence of excess pore pressure. In particular, based on their experimental observations on the permeability reduction, induced pore pressure and flow behavior due to compaction localization, Holcomb and Olsson (2003) argued that the induced pore pressure might play an impeding effect on the propagation of compaction bands. Despite these limited experimental progresses, there has been no conclusive consensus established, based upon systematic, rigorous theoretical examinations, to guide our understanding of the intricate interactions between pore fluid and deformation bands in sandstone.

To advance this line of research, we extend our previous multiscale study of compaction bands in high-porosity sandstones under dry conditions (Wu et al., 2018a) in conjunction with a recent developed

fully coupled hydro-mechanical scheme (Guo and Zhao, 2016c) for modeling of saturated sandstone. The hierarchical multiscale approach solves the boundary value problem (BVP) with finite element method (FEM), and obtains the required material constitutive responses from direct DEM computations of the representative volume elements (RVEs) embedded at each Gauss integration point of the finite element mesh. As such, it helps bypass the need for pre-assumed phenomenological constitutive law as is mandatory in conventional continuum modeling. A typical hydro-mechanical coupling problem for saturated sandstone is solved by adopting a standard  $\mathbf{u}$ - $p$  formulation. The effective stress is derived straightforwardly from the DEM solution, and is superimposed with the pore pressure to obtain the total stress in the governing equation according to the Terzaghi's effective stress principle. Based on the new multiscale hydro-mechanical framework, we will first compare the predictions of globally drained tests on a saturated high-porosity sandstone specimen with a purely dry corresponding case. The focus will then be placed on the evolution of induced pore pressure during globally undrained loading and its interplay with the initiation, development and possible transition of compaction bands.

## 2. Methodology

Fig. 1 presents a schematic of the solution scheme for multiscale modeling of hydro-mechanical coupling in saturated granular rocks. The macro domain of a BVP of saturated granular rock (exemplified by a biaxial compression test) is discretized by FEM. A RVE is embedded at each Gauss integration point of the FE mesh. It receives deformation and pore pressure from FEM as boundary conditions and uses DEM to solve for a local solution. From the deformed RVE the required material responses including stress, tangential stiffness and updated pore pressure are extracted and returned to FEM as updates. These RVE updates are then used by FEM to solve for a global solution to provide updated deformation and pore pressure at each Gauss point for the corresponding RVE. Detailed equations and algorithms of the hierarchical multiscale approach involving hydro-mechanical coupling could be found in (Guo and Zhao, 2014, 2016c). Nevertheless, there are various aspects needing to be improved on this promising new method. Notable recent efforts include the examination of the size and variability of RVE (Guo and Zhao, 2014, 2016a; Shahin et al., 2016), the computational performance (Argilaga et al., 2018) and the mesh dependency of the solution (Desrues et al., 2019). The applications of similar approaches in multiscale modeling of fracture can be found in (Talebi et al., 2014; Budarapu et al., 2014). To avoid unnecessary repeat, only the essential ingredients are briefly introduced in the following.

The Terzaghi's effective stress principle suggests that the total stress  $\sigma_{ij}$  in a saturated porous medium is composed of the effective stress  $\sigma'_{ij}$  carried by the solid skeleton and the pore pressure  $p$  sustained by the pore fluid:

$$\sigma_{ij} = \sigma'_{ij} + \alpha p \delta_{ij} \quad (1)$$

where  $\alpha$  is the Biot coefficient and  $\delta_{ij}$  is the Kronecker delta. For simplicity, the Biot coefficient is set to unity  $\alpha = 1$  in this study following Baud et al. (2015) who obtained a Biot coefficient very close to 1 for Bleurswiller sandstone (a high-porosity sandstone with compaction bands observed). In the hierarchical multiscale modeling scheme, the effective stress  $\sigma'_{ij}$  is directly attainable from the DEM solution of the RVE, and the pore pressure  $p$  is obtained based on mass conservation of the fluid phase:

$$[k_{ij}(-p_j + \rho_f b_j)]_{,i} + \alpha u_{i,i} + \frac{n}{K_f} \dot{p} = 0 \quad (2)$$

where  $k_{ij}$  is the permeability tensor (in the unit of  $\text{m}^2/(\text{Pa}\cdot\text{s})$ ),  $\rho_f$  is the density of the pore fluid,  $b_j$  is the body force due to gravity (ignored in this study),  $u_{i,i}$  is the volumetric strain of the solid skeleton,  $n$  is the porosity of the mixture and  $K_f$  is the bulk modulus of the fluid. The permeability is treated as isotropic for simplicity, i.e.  $k_{ij} = \frac{k}{\mu_f} \delta_{ij}$ , where  $k$

is the scalar permeability and  $\mu_f$  is the dynamic viscosity of the fluid. A superimposed dot means time derivative of the variable. In the above equation, the solid grain is assumed incompressible.

The scalar permeability  $k$  is assumed to be a function of porosity  $n$  based on the Kozeny–Carman equation, which has been widely adopted to predict the permeability of sands and sandstones (Andrade and Borja, 2007; Guo and Zhao, 2016c):

$$k = \frac{\bar{d}^2 n^3}{72\tau^2(1-n)^2} \quad (3)$$

where  $\bar{d}$  is the average diameter of the grains,  $\tau$  is the tortuosity. The tortuosity  $\tau$  is taken as 2.5 based on experimental (Gomez et al., 2010) and tomographic analyses (Sun et al., 2011) on clean sandstones. The pore fluid is assumed as water here with  $K_f = 2.2$  GPa and  $\mu_f = 8.9 \times 10^{-4}$  Pa·s at room temperature. With  $\bar{d} = 0.5$  mm and an initial porosity  $n_0 = 0.326$ , the high-porosity RVE in this study has an initial permeability  $k_0 = 4.2 \times 10^{-11}$   $\text{m}^2$ .

### 2.1. Biaxial compression tests

We have carried out a multiscale modeling of compaction bands in sandstone under biaxial compression for the dry case (Wu et al., 2018a). A similar model setup is adopted here to examine the coupled hydro-mechanical effects for saturated sandstones. The problem domain and the mesh discretization are illustrated in Fig. 2a. Each element contains 8 displacement nodes and 4 pressure nodes. A reduced integration scheme with 4 RVEs for each finite element is adopted to save computational cost. The top and bottom boundaries can be either smooth with no lateral constrains (for most cases, as presented in Fig. 2a) or totally rough with no lateral displacement (for a special case in Section 4.3.3). In the smooth case, the center of the bottom boundary is fixed to render converged solutions. The specimen is loaded along the vertical direction by applying a uniform vertical displacement on the top boundary with a nominal axial strain rate  $\dot{\epsilon}_1 = -1 \times 10^{-5} \text{s}^{-1}$  (by following the experiments by Baud et al. (2015)). A constant confining stress  $\sigma_3$  is applied on both the left and right boundaries which are supposed to be impervious. The top and the bottom boundaries can be either fully permeable or impervious, to achieve a globally drained or undrained condition, respectively. Local drainage at any point of the material domain is allowed in either condition. The time step of the simulation is set to  $\Delta t = 10$  s to maintain a quasi-static loading condition.

### 2.2. RVE for high-porosity sandstones

Grain crushing is considered a key mechanism in the formation of compaction bands in laboratory experiments on sandstones (Baud et al., 2004; Fortin et al., 2006). However, field observations indicate that compaction bands may form with much fewer and less intense particle breakage at lower geological confining pressure (Aydin and Ahmadov, 2009; Deng and Aydin, 2012). Compaction bands have indeed been reproduced for high-porosity sandstones earlier by the authors without considering particle crushing, where pore collapse and debonding were identified as controlling factors (Wu et al., 2018a). More recently, 'fracture-like' breakouts, also called emptied compaction bands (Haimson and Kovacich, 2003), have been reproduced around a borehole with a high-porosity RVE mimicking field sandstone (Wu et al., 2017, 2018b). A similar high-porosity RVE with periodic boundaries, consisting of 749 non-crushable circular particles, is adopted in this study. Nevertheless, we note that the high-porosity structure employed here may be merely one of many possible microstructures in sandstones that could trigger compaction bands.

The high-porosity RVE, as illustrated in Fig. 2b, is generated by removing some pre-inserted larger particles and rattlers (particles with less than one contact) in the generated DEM packing. The stability of

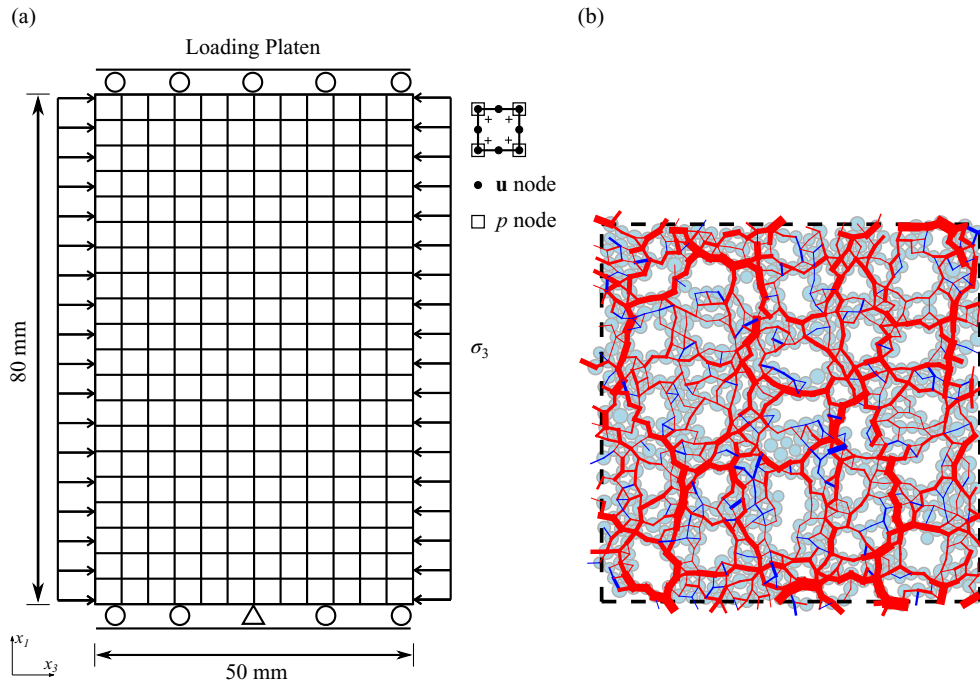


**Fig. 2.** (a) Finite element discretization and boundary conditions for multiscale hydro-mechanical modeling of biaxial compression on saturated sandstone. (b) Initial RVE packing for the high-porosity sandstone (porosity: 0.326) under an isotropic confining pressure of 40 MPa. The dashed rectangle marks the periodic boundary of the packing. Red and blue lines indicate the normal interparticle contact forces (red for compressive contacts and blue for tensile contacts). (For interpretation of the references to colour in this figure legend, the reader is referred to the web version of this article.)

**Table 1**  
The parameters of the DEM particles.

Parameter	Value
Particle radii $r$ (mm)	0.2–0.3
Particle density $\rho$ (kg/m <sup>3</sup> )	2650
Interparticle friction angle $\phi$ (°)	35
$E_c$ (GPa)	950
$\nu_c$	1.0
Cohesion strength $c$ (GPa)	6.8

**Table 2**  
The properties of the high-porosity RVE.

Property	Value
Initial porosity $n_0$	0.326
Initial permeability $k_0$ (m <sup>2</sup> )	$4.2 \times 10^{-11}$
Uniaxial compression strength UCS (MPa)	24.9
Young's modulus $E$ (GPa)	11.0

the structure is maintained by applying interparticle bonds before the removal of any particles. The bonds are applied based on a bonded contact model with a linear force–displacement law and a Coulomb-type friction criterion. The normal and the tangential contact stiffnesses are derived as  $k_n = E_c \times \frac{2r_1r_2}{r_1+r_2}$  and  $k_t = \nu_c k_n$ , respectively, where  $r_1$  and  $r_2$  are the radii of the two contacting particles,  $E_c$  and  $\nu_c$  are two user-defined parameters. The maximum tensile force is defined as  $F_n^{\max} = c \min(r_1, r_2)^2$  and the maximum tangential force as  $F_t^{\max} = c \min(r_1, r_2)^2 + F_n \tan(\phi)$ , where  $c$  is the cohesion strength and  $\phi$  is the interparticle friction angle. If either of the two thresholds is exceeded, the bond will break leaving a pure frictional contact afterwards (i.e.,  $F_t \leq F_n \tan(\phi)$ ). The calibrated microparameters for the DEM particles are summarized in Table 1. The radii of the particles are linearly distributed from 0.2 to 0.3 mm, following the well-sorted Berea sandstone with a mean radius of 0.25 mm (Haimson and Kovacich, 2003). The particle density  $\rho$  and the interparticle friction angle  $\phi$  are common values in DEM simulations of sands and sandstones. The parameters for stiffness and cohesion are calibrated such that the modeled sandstone reaches a uniaxial compressive strength (UCS) of 24.9 MPa and Young's modulus ( $E$ ) of 11.0 GPa, which are in agreement with two sandstones, namely the Berea sandstone with  $UCS = 24 \pm 2$  MPa (Haimson and Kovacich, 2003), and the Mansfield sandstone with  $UCS = 22.4 \pm 0.5$  MPa and  $E = 9.6 \pm 0.1$  GPa (Haimson and Lee, 2004). Properties of the prepared high-porosity RVE as presented in Fig. 2b are summarized in Table 2.

### 3. Validation of equivalence: drained versus dry tests

In micromechanics-based modeling, dry tests have long been regarded to yield similar responses as drained tests for granular media. However, the equivalence has never been validated numerically. In this section, we will examine and validate if the predictions from the two types of loading conditions can be indeed considered equivalent. The same specimen discretized by the same mesh (Fig. 2a) and subjected to the same confining pressure  $\sigma_3 = 30$  MPa is examined under dry and saturated but drained conditions, respectively. For the dry test, only the displacement nodes are effective. The drained simulations consider presence of pore pressure with both top and bottom boundaries of the sample in Fig. 2a permeable.

#### 3.1. Global responses

The global responses of the two tests, in terms of the axial effective stress  $\sigma_1'$  and the global incremental normalized debonding number  $N^g$  within the specimen (normalized by the initial contact number within the specimen), are plotted in Fig. 3.  $N^g$  is comparable to the acoustic emission rate which is widely adopted in the experimental studies of rock as an indicator of the damage process. The red solid lines stand for the dry case, while the blue dashed ones represent the drained case. Fig. 3 shows that the pre-peak responses of the drained case and the dry case are almost identical and their post-peak behaviors remain rather close, despite the fluctuations. The fluctuation of  $\sigma_1'$  is characterized by gradual build-up and episodic drops. The build-up of  $\sigma_1'$  corresponds to the valley of  $N^g$ , while the episodic stress drop is accompanied by a pulse of  $N^g$ , which is corresponding to a cluster of local damage zone perpendicular to  $\sigma_1'$  during the thickening in width of the compaction

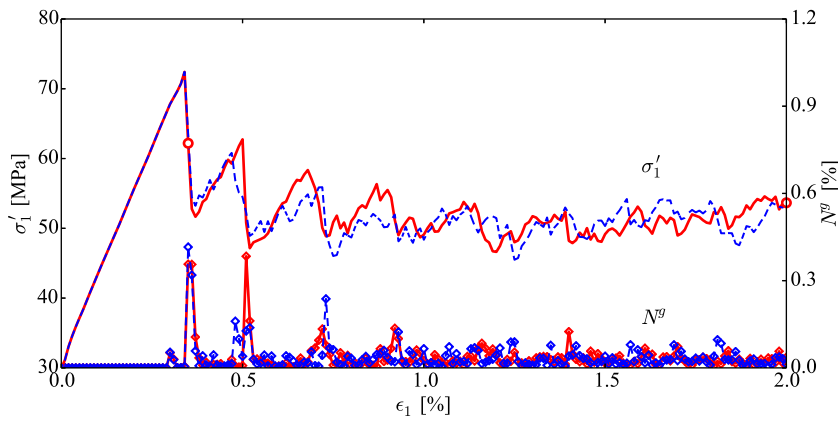


**Fig. 3.** A comparison of the global responses between the dry case (red solid lines) and the drained case (blue dashed lines) under  $\sigma_3 = 30$  MPa, in terms of axial effective stress  $\sigma'_1$  and global incremental normalized debonding number  $N^g$  (normalized by the initial contact number within the specimen). (For interpretation of the references to colour in this figure legend, the reader is referred to the web version of this article.)

band. This is a typical feature in the development of compaction bands which has been reported in numerous experimental and numerical studies (Baud et al., 2004; Wu et al., 2018a).

### 3.2. Initiation and development of compaction bands

Contours of the local accumulated normalized debonding number within an RVE ( $N^l$ , normalized by the initial contact number in an RVE), the accumulated deviatoric strain ( $\epsilon_q = \sqrt{(\epsilon_{11} - \epsilon_{33})^2 + 4\epsilon_{13}^2}$ ), the accumulated volumetric strain ( $\epsilon_v = \epsilon_{11} + \epsilon_{33}$ , where compression is taken as positive), and the average particle rotation ( $\theta$ ) for the dry case and the drained case at the initial stage of the compaction band ( $\epsilon_1 = 0.35\%$ ) and the final stage ( $\epsilon_1 = 2.0\%$ ) (marked as open red circles in Fig. 3) are plotted in Fig. 4 for comparison. While heterogeneity and uncertainty in parameters play an important role during the failure process (Hamdia et al., 2017), a specimen with two initial weak points (marked as white dots in Fig. 4a, with a reduced cohesion strength of 80% of the normal value) is adopted in this study to reproduce a clear band pattern and highlight the possible transitions. The initiation of compaction bands from local weak points is supported by experimental results (Fortin et al., 2006) and has been reproduced in our previous numerical simulations (Wu et al., 2018a). The first two rows in Fig. 4 show the initiation of the compaction bands from the weak points and their penetration through the specimen along the horizontal direction in both cases. Subsequently, the compaction bands expand along the vertical direction and become thicker in width as shown in the following figures. The thick compaction bands at the final stage when  $\epsilon_1 = 2.0\%$  are plotted in the last two rows. The thickening in width of the compaction bands is similar to the so-called ‘compaction front’ observed in experiments (Olsson, 2001).

The contours of key local variables shown in Fig. 4 indicate that both dry and drained cases offer rather similar simulations on the initiation and the development of compaction bands, which is consistent with their similar global responses in Fig. 3. Since the computational cost of a fully coupled drained simulation is considerably higher than that of a dry test, it appears to be reasonable to treat a dry simulation as equivalent to the corresponding drained case.

## 4. Multiscale modeling of undrained biaxial compression

Compaction bands have been observed under  $\sigma_3 = 30$  MPa in drained and dry cases in Section 3. The in-band volumetric strain reaches as high as 10% at the final stage when  $\epsilon_1 = 2.0\%$  (see Fig. 4k and o). Significant volumetric contraction may cause great excess pore pressure and act as an important fluid source if the specimen is saturated and drainage is constrained. Holcomb and Olsson (2003) calculated an induced pore pressure of 0.4 MPa at the formation of ‘compaction fronts’ in their drained experiment and pointed out that the pressure might be comparable to the driving stresses and affect the

compaction process in a rapid loading or a reservoir scale problem. The fully coupled hydro-mechanical multiscale approach presented in previous sections enables us to perform simulations of a saturated sample under undrained conditions, to thoroughly explore the interplay between pore pressure change and evolution of compaction or other deformation bands. Since compaction bands are observed under a confinement of 30 MPa in our drained/dry simulations, a globally undrained simulation of the same specimen under  $\sigma_3 = 30$  MPa is conducted first to demonstrate the alteration of initial failure mode due to induced pore pressure. Two more undrained simulations under  $\sigma_3 = 40$  MPa are presented thereafter to demonstrate the transitions of compaction bands induced by pore pressure under smooth and rough loading conditions, respectively.

### 4.1. Pore pressure induced alteration of initial failure mode under undrained condition

#### 4.1.1. Global responses of the specimen

The global responses of the specimen subjected to undrained shear under  $\sigma_3 = 30$  MPa are plotted in Fig. 5a, in terms of the axial effective stress  $\sigma'_1$ , the mean induced excess pore pressure  $p$  and the global incremental normalized debonding number  $N^g$  within the specimen. The entire process can be divided into the pre-peak stage and the post-peak stage based on the evolution of  $\sigma'_1$ :

1. Stage I: pre-peak stage. The pre-peak stage of the undrained specimen features an almost elastic response with linear increase in both  $\sigma'_1$  and  $p$  and negligible debonding. The several debonding events observed in this stage occur mainly in the two pre-existing weak points (marked as two white points in Fig. 5b), which remain too small and local to induce any notable failure of the whole specimen.
2. Stage II: post-peak stage. Starting from the peak, the specimen experiences a dramatic drop of  $\sigma'_1$  and a burst of  $N^g$ , which is induced by the initiation of failure of the specimen and the formation of an inclined band (see Fig. 5b–e).  $p$  starts to build up steadily with an increasing rate before  $\epsilon_1 = 1.0\%$  due to the compaction nature of this band (see Fig. 5d). Afterwards,  $p$  continues to build up but at a decreasing rate before reaching an almost constant value after  $\epsilon_1 = 2.0\%$ . Notably, the post-peak responses of  $\sigma'_1$  and  $N^g$  in the undrained test are apparently different from those in the drained test. Instead of episodic peaks and valleys shown in the drained test, the post-peak  $\sigma'_1$  decreases monotonically with marginal fluctuations while  $N^g$  maintains a small value close to 0 with the steady development of the inclined band. Both  $\sigma'_1$  and  $p$  tend to reach constant values at large strains. It is also noted that at the final stage,  $\sigma'_1$  reduces to a value of around 20 MPa and the effective confining pressure ( $\sigma'_3 = \sigma_3 - p$ ) is around 5 MPa.

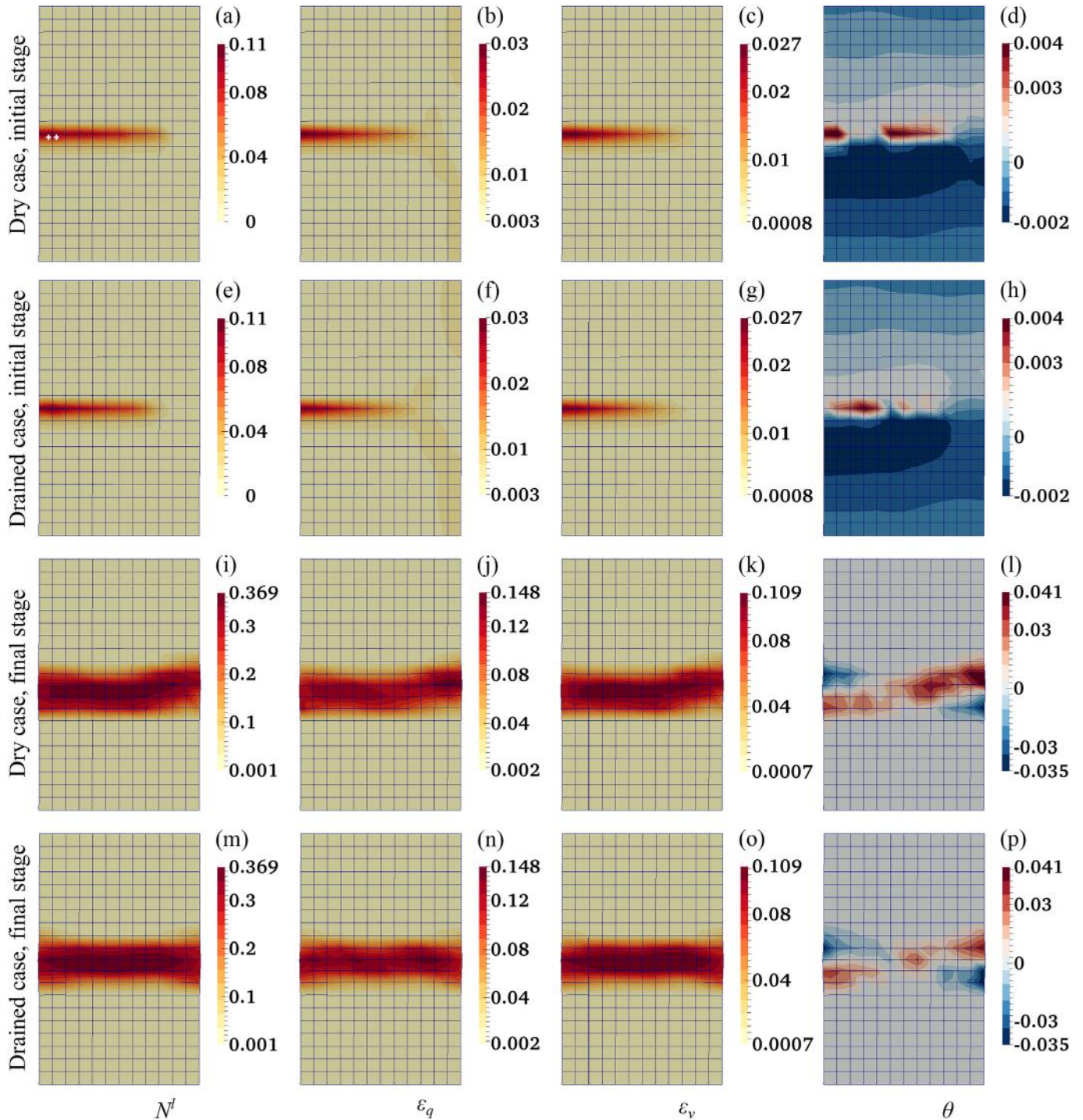


**Fig. 4.** Comparison of the dry case and the drained case under  $\sigma_3 = 30$  MPa in terms of the local accumulated normalized debonding number  $N^l$  (normalized by initial contact number in a RVE), the accumulated deviatoric strain  $\epsilon_q$ , the accumulated volumetric strain  $\epsilon_v$  and the average particle rotation  $\theta$  at the initial and final stages of the compaction bands.

#### 4.1.2. Band initiation and development

Details of the initial and the final state of the inclined band are plotted in Fig. 5b–i, in terms of the local accumulated normalized debonding number  $N^l$ , the deviatoric strain  $\epsilon_q$ , the volumetric strain  $\epsilon_v$  and the average particle rotation  $\theta$ . Consistent failure patterns could be identified from the contours of the four variables. Fig. 5b–e show the initiation of the inclined band from the pre-existing weak points with a dip angle of  $38^\circ$  with respect to the horizontal direction. Fig. 5f–i illustrate the final state of the band of the same dip angle but with intensified damage, enhanced particle rotation and larger deviatoric and

volumetric strains than those at the initial state. Specifically, the maximum values of  $N^l$  and  $\epsilon_v$  increase by 2–3 times, and those of  $\epsilon_q$  and  $\theta$  even increase by an order of magnitude. The evolutions of the four variables demonstrate significant increase in shear components over this deformation during the increase in axial strain and the build-up of pore pressure.

#### 4.1.3. Comparison with the dry/drained case

Field investigations commonly classify deformation bands in high-porosity sandstones kinematically into compaction band (CB), shear-

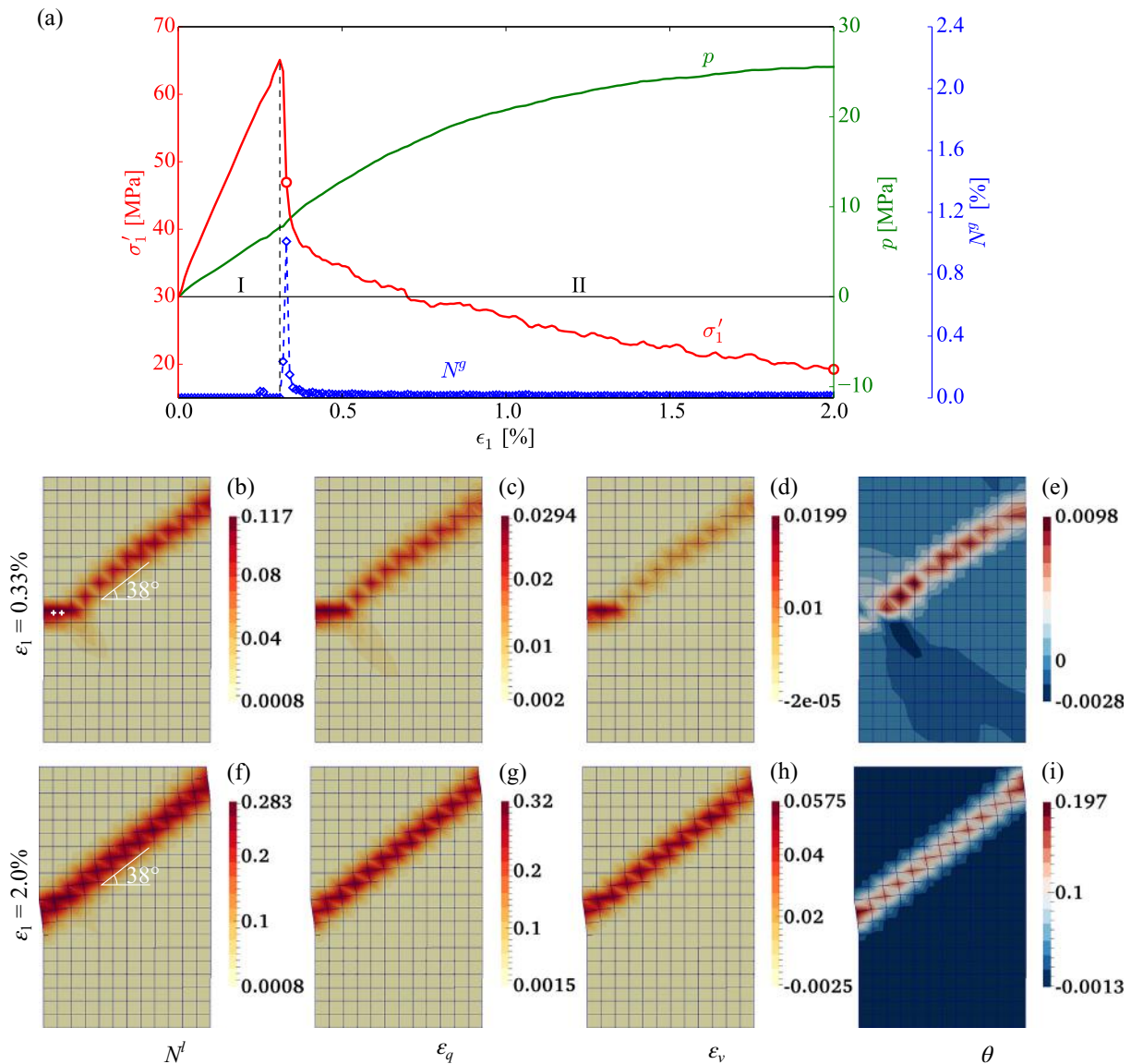
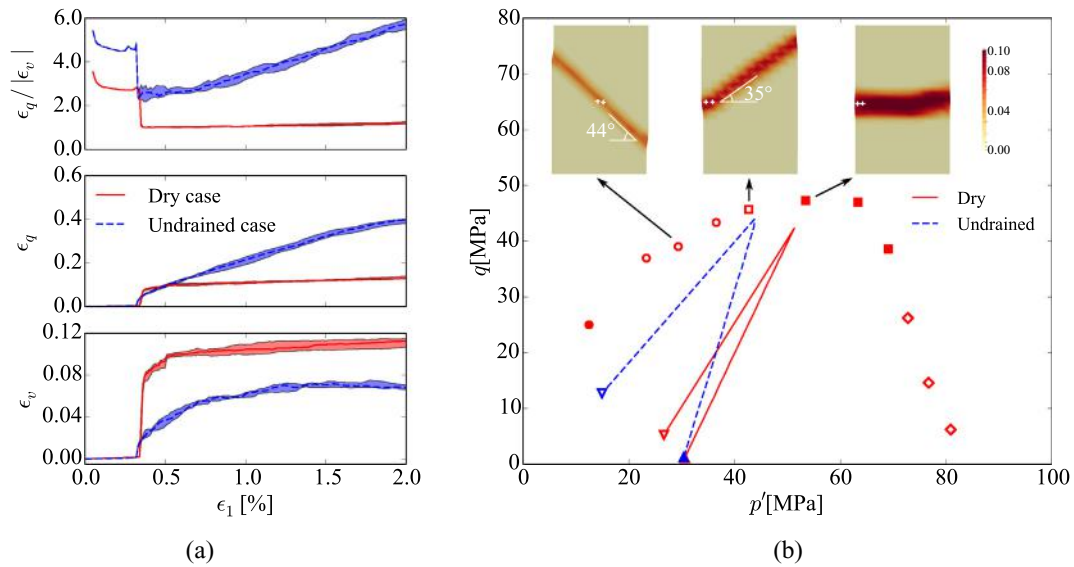


Fig. 5. Multiscale predictions of a saturated high-porosity sandstone specimen subjected to undrained biaxial compression under  $\sigma_3 = 30$  MPa. (a) Evolutions of the axial effective stress  $\sigma'_1$ , the mean excess pore pressure  $p$  and the global incremental normalized debonding number  $N^g$  with increased axial strain; (b–i) The initial and final failure patterns of the specimen shown by contours of the local accumulated normalized debonding number  $N^l$ , the deviatoric strain  $\epsilon_q$ , the volumetric strain  $\epsilon_v$  and the average particle rotation  $\theta$ .

enhanced compaction band (SCB) and compactive shear band (CSB) based on the ratio of shear to compaction displacement (S/C) (Fossen et al., 2017; Soliva et al., 2013). Since it is difficult to measure S/C directly in laboratory experiments, the differences in terms of deviatoric and volumetric strains among different types of deformation bands have been investigated instead with X-ray tomography and digital image correlation in some experimental studies (Charalampidou et al., 2011, 2014). The different local strain features have also been analyzed in numerical simulations of deformation bands (Wu et al., 2018a). The ratio of deviatoric strain to volumetric strain ( $\epsilon_q / |\epsilon_v|$ ) of the in-band RVEs is adopted in this study to analyze the failure mode and its evolution. Since only the post-failure value of strain ratio  $\epsilon_q / |\epsilon_v|$  is of interest, the absolute value of  $\epsilon_v$  is adopted here to avoid the abrupt change caused by the slight dilation due to elastic unloading. After all, the dilation band is rare for high-porosity sandstones and not a focus of this study. Note that negative  $\epsilon_v$  (slightly larger than  $-0.005$ ) in Figs. 5 and 7 for some areas outside the band are indeed observed.

The evolutions of  $\epsilon_q / |\epsilon_v|$ ,  $\epsilon_q$  and  $\epsilon_v$  of 10 selected in-band RVEs in

the dry and the undrained cases are illustrated in Fig. 6a for comparison. As introduced in Section 3, a compaction band is observed in the dry case. The corresponding  $\epsilon_q$  and  $\epsilon_v$  of the in-band RVEs in the dry case show clear surges at the initiation of the band and keep almost constant during the thickening stage. The evolution of  $\epsilon_q / |\epsilon_v|$  displays a constant initial value of around 3.0, an apparent drop at the initiation of the compaction band followed by a constant value close to 1.0. The pre-failure value of  $\epsilon_q / |\epsilon_v|$  is related to the Poisson's ratio of the material, while the small post-failure value confirms the failure mode as CB in nature. In contrast to the dry case, an inclined band with a dip angle of  $38^\circ$  is observed in the undrained case.  $\epsilon_v$  presents a gradual increase followed by a plateau in the post-failure stage, whereas  $\epsilon_q$  displays a continuous linear increase. The pre-failure value of  $\epsilon_q / |\epsilon_v|$  is larger than that for the dry case due to the decrease of  $\sigma'_3$  induced by pore pressure build-up, which further results in a larger  $\epsilon_q$ . The failure mode could be analyzed with the post-failure evolution of  $\epsilon_q / |\epsilon_v|$ , whose value evolves from around 2.5 to around 6.0 at the final stage, indicating a gradual transition of failure mode from SCB to CSB.



**Fig. 6.** (a) The evolutions of strain ratio  $\epsilon_q/|\epsilon_v|$ , deviatoric strain  $\epsilon_q$  and volumetric strain  $\epsilon_v$  of 10 selected in-band RVEs in the dry and undrained cases under  $\sigma_3 = 30$  MPa. The lines in the middle are the medians, while the lower and upper bounds of the filled areas are the first and the third quartiles, respectively. (b) The effective stress paths of the typical in-band RVEs. The upward solid triangle marks the start of the stress paths and the downward empty triangles mark the end. The failure loci obtained from pure DEM modeling on the RVE are presented by the isolated red markers. The different markers are indicative of bounds for different failure modes: solid circles for dilative shear band (not a focus of this study), empty circles for CSB, empty square for SCB, solid square for CB and empty diamonds for distributed compaction failure (without clear band pattern, not a focus of this study). The inset shows different deformation patterns obtained from multiscale modeling in dry biaxial compression tests. (For interpretation of the references to colour in this figure legend, the reader is referred to the web version of this article.)

The major difference between the dry case and the undrained case is the build-up of  $p$ . The distinctively different failure modes observed in the two cases could be better explained with the help of effective stress paths in the  $q$ - $p'$  plane (where  $q$  and  $p'$  are two effective stress invariants commonly used in soil mechanics:  $q = \sqrt{(\sigma_{11} - \sigma_{33})^2 + 4\sigma_{13}^2}$  is the deviatoric stress and  $p' = \frac{\sigma_{11} + \sigma_{33}}{2}$  is the mean effective stress). The effective stress paths of the typical in-band RVEs in the two cases have been comparatively plotted in Fig. 6b. The failure loci of the RVEs solved by pure DEM simulations under biaxial compression are plotted for reference with different markers indicating the transition of failure mode with the increase in mean effective stress. As indicated by the insets, the open square marks the failure as SCB and the solid squares indicates the failure as CB under corresponding confinement in a dry biaxial compression test. Due to the increase in pore pressure  $p$ , the effective stress path for the undrained case deviates to the left side of the corresponding one for the dry case and the failure occurs at a lower  $p'$ , which leads to the change of the initial failure mode from CB in the dry case to SCB in the undrained case.

#### 4.2. Pore pressure induced transition of compaction band

Section 4.1 presents clearly that the induced pore pressure may cause the reduction in mean effective stress and change the failure mode from CB (in the dry case) to SCB (in the undrained case). It is intuitive to expect that the initial failure mode may be CB under undrained condition so long as  $\sigma_3$  is high enough, and the failure mode may shift from CB to CSB with the build-up of pore pressure under continuous loading. To examine if it is the mean effective stress rather than the total mean stress that serves as a controlling factor of the failure mode in sandstone, we further perform numerical simulations of the same specimen with  $\sigma_3 = 40$  MPa, under both dry and undrained conditions. As expected, the dry case presents a typical CB similar to the observations in Fig. 4. The failure mode transition in the undrained case is more interesting and presented below.

##### 4.2.1. Undrained global responses

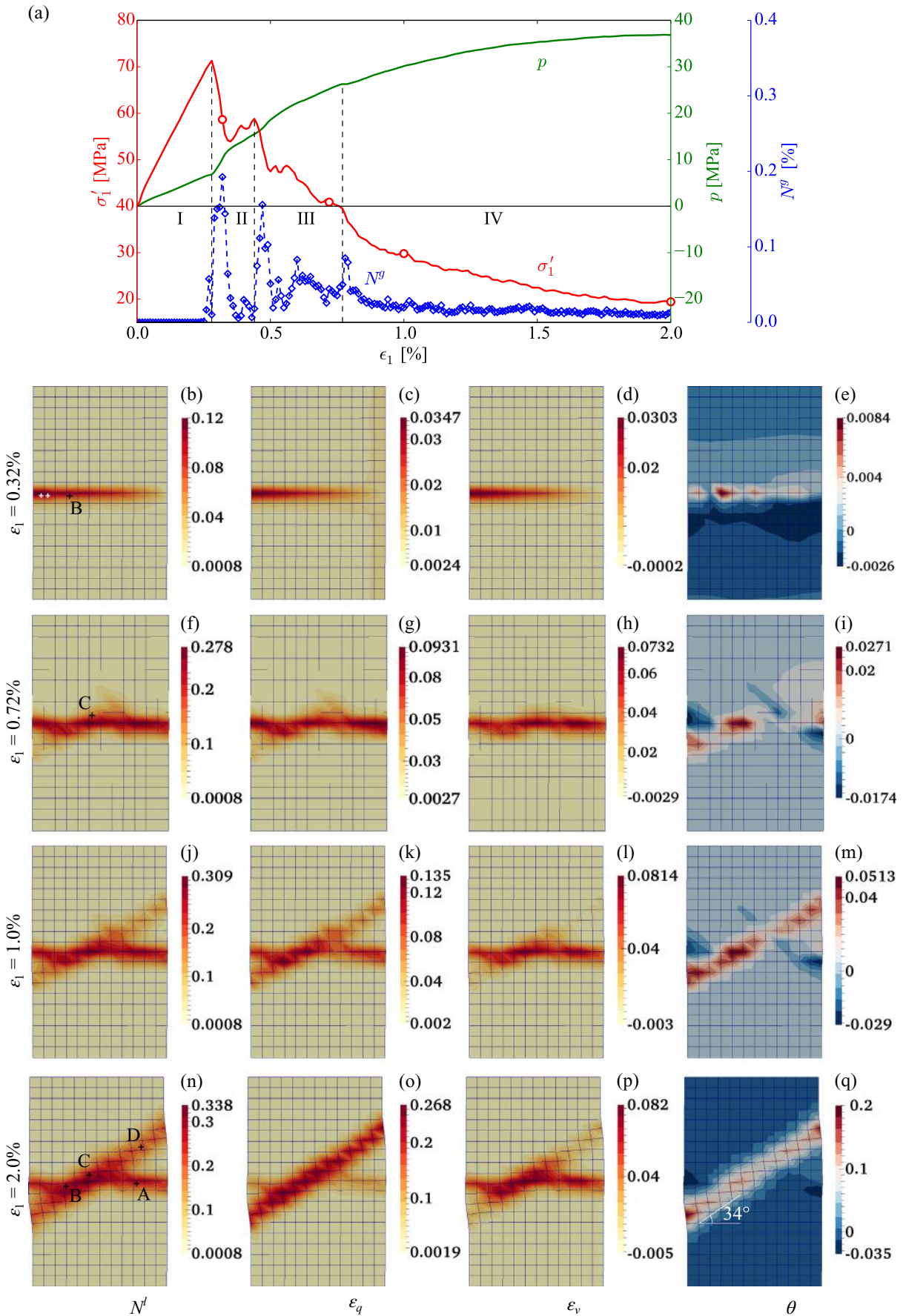
The global responses of the specimen subjected to undrained

compression under  $\sigma_3 = 40$  MPa, in terms of  $\sigma_1'$ ,  $N^g$  and  $p$ , are plotted in Fig. 7a. The simulation stops at  $\epsilon_1 = 2.0\%$  when the three quantities approach steady state values. The entire process of the undrained responses could be divided into four stages according to the figure:

1. Stage I: elastic stage. This stage presents linear increases in both  $\sigma_1'$  and  $p$  with the axial strain accompanied with negligible  $N^g$ . The peak of  $N^g$  at the end of this stage is mainly due to the damage at the two weak points (marked as the two white dots in Fig. 7b).
2. Stage II: CB stage. This stage features the initiation and further development of a CB. The initiation of the CB is characterized by a stress drop, a notable increase in  $p$  and a burst of debonding events. The CB penetrates through the specimen at the end of this stage.
3. Stage III: transition stage. The development of CB appears to mature at the beginning of this stage when intense damage occurs. A steady drop of  $\sigma_1'$  is noted without pulling-back due to the accumulation of  $p$ , in contrast to the episodic peaks and valleys in the dry case. The CB gradually becomes wiggly in this stage, giving birth to a later CSB at some kinks of the CB (see Fig. 7f-i).
4. Stage IV: CSB stage. This stage features the formation and extension of a clear CSB.  $N^g$  presents a small peak at the beginning of this stage and stays low afterwards. The small peak is corresponding to the formation of a CSB cutting through the specimen, with an approximate dip angle of  $34^\circ$  to the horizontal.  $\sigma_1'$  decreases quickly at the beginning of the stage and approaches a steady state towards the end.  $p$  increases at a decreasing rate and approaches a steady state at the end. The CSB develops steadily as the increase in axial strain and is further intensified to be clearly identifiable at the final state.

##### 4.2.2. Transition of failure modes

The contours of  $N^t$ ,  $\epsilon_q$ ,  $\epsilon_v$  and  $\theta$  at four selected axial strain levels (marked as red open circles in Fig. 7a) are plotted in Fig. 7b-q to illustrate the transition of failure modes in the undrained test. Fig. 7b-e present the typical failure mode in Stage II. A horizontal CB could be consistently identified from the contours of  $N^t$ ,  $\epsilon_q$  and  $\epsilon_v$ . The average particle rotation is rather small and displays a rotating-into-band pattern. The transition from CB to CSB in Stage III is illustrated in Fig. 7f-i.



(caption on next page)

**Fig. 7.** Pore pressure induced transition of compaction bands (triggered by the pre-inserted weak points with a reduced cohesion strength, see the two white dots in (b)) subjected to undrained loading under  $\sigma_3 = 40$  MPa. (a) The global responses in terms of  $\sigma_1^t$ ,  $N^t$  and  $p$  with increased  $\epsilon_1$ . (b–q) Contours of  $N^t$ ,  $\epsilon_q$ ,  $\epsilon_v$  and  $\theta$  at four typical axial strain levels (see the four open circles in (a)) showing the transition of compaction band.

Notably, a slightly inclined band with a dip angle of  $34^\circ$  starts to branch from the CB formed in Stage II, instead of the continuous thickening of the CB in the dry case. The wiggly band pattern at this stage is similar to the tortuous CB in experiments (Baud et al., 2015) and the wavy CB in field outcrops (Liu et al., 2015).

The formation of a CSB cutting through the specimen marks the start of Stage IV. The CSB could be clearly identified from the contours of  $N^t$ ,  $\epsilon_q$  and  $\theta$  as shown in Fig. 7j, k and m. Due to small compaction involved in this CSB, its form is relatively vague in the contour of  $\epsilon_v$  as shown in Fig. 7l. The failure is dominated by the development of CSB in Stage IV. The final failure pattern at  $\epsilon_1 = 2.0\%$  is presented in Fig. 7n–q.  $\theta$  and  $\epsilon_q$  are more dominant in the CSB than in the CB at this stage. However, it is evident that  $\epsilon_v$  dominates in the CB than in the CSB. Interestingly, the intensities of the two bands are comparable in the contour of  $N^t$ , indicating the occurrence of significant damages in both bands.

4.2.3. Failure mode analyses based on microscopic features

The multiscale approach enables us to make a cross-scale analysis to identify the microstructural mechanisms linked to the evolution of macro bands during the four global stages as shown in Fig. 7a. To this end, we choose several RVEs at different locations with distinct deformation features for analysis. Indeed, the RVEs within the band area at the final state can be classified into 4 types to analyze the evolution of the failure mode. Type A: RVEs located only in the initial CB; Type B: RVEs in the intersection of the initial CB and the final CSB; Type C: RVEs located in the final CSB which initially fail in the transition stage; Type D: RVEs located only in the CSB. The typical RVEs of each type are marked by black dots in Fig. 7. Note that RVEs of Type B differ from Type C in that Type B RVEs fail initially in Stage II, while Type C RVEs fail first in Stage III.

In Fig. 8a we compare the evolutions of the strain ratio  $\epsilon_q/|\epsilon_v|$ , the deviatoric strain  $\epsilon_q$  and the volumetric strain  $\epsilon_v$  for the four types of RVEs. A logarithmic scale is adopted for  $\epsilon_q/|\epsilon_v|$  for better presentation. RVEs of Type A and Type B mainly fail during Stage II. Their post-failure values of  $\epsilon_q/|\epsilon_v|$  drop to close to 1.0 in Stage II, which agrees

with the compaction band identified from Fig. 7b–e. Type C and Type D RVEs depict an obvious surge for  $\epsilon_q/|\epsilon_v|$  in Stage II, due to an increase of excessive pore pressure and hence a drop of effective stress at these RVEs which induces a slight volume rebound and increase in shear strain. Since the initial values for both quantities are extremely small at these RVEs, the above changes give rise a significant increase in  $\epsilon_q/|\epsilon_v|$ . Type C RVEs fail at Stage III and their curves are relatively more scattered at failure than other types, which is related to the occurrence of different failure modes in this stage. The fact that some of these Type C RVEs fail as CB and others fail as SCB reflects the transition of failure mode in Stage III. Rather distinct from the other 3 types, Type D RVEs fail at Stage IV with an obvious peak for  $\epsilon_q/|\epsilon_v|$ . The largest post-failure values among these types agree with the features of CSB. It is interesting to note that there are gradual increases in  $\epsilon_q/|\epsilon_v|$  at Stage IV for Type B and Type C RVEs, suggesting a gradual transition of the failure mode from CB or SCB first and then to CSB. This is a natural consequence caused by the dominance of shear in the inclined band in stage IV (see the increase of  $\epsilon_q$  but the almost constant  $\epsilon_v$ ).

The effective stress paths of the typical RVEs of each type are plotted in Fig. 8b (see their locations marked with black dots in Fig. 7). The failure loci obtained from pure DEM simulations under dry biaxial compression condition are also presented for reference. See the different use of markers in Fig. 6. It is noted that the failure of Type A and Type B RVEs occur at the high mean effective stress  $p'$  regime (solid squares) though the corresponding  $p'$  for the same  $q$  is smaller than that from the drained loading path (the black dashed line) due to the induced pore pressure  $p$ . This is consistent with the observed CB at stage II. Due to continuous accumulation of  $p$ , Type C and Type D RVEs fail at lower  $p'$ . The selected Type C RVE fails at medium  $p'$  regime (open square) and the failure mode is identified as SCB. Type D RVE fails at an even lower  $p'$  (open circles), leading to a failure mode of CSB at Stage IV.

The failure modes in the undrained case are evidently complicated due to the change of pore pressure. Nevertheless, the above analyses indicate that the initial failure mode of a RVE is controlled by the mean effective stress, so that it may vary at different locations in a specimen

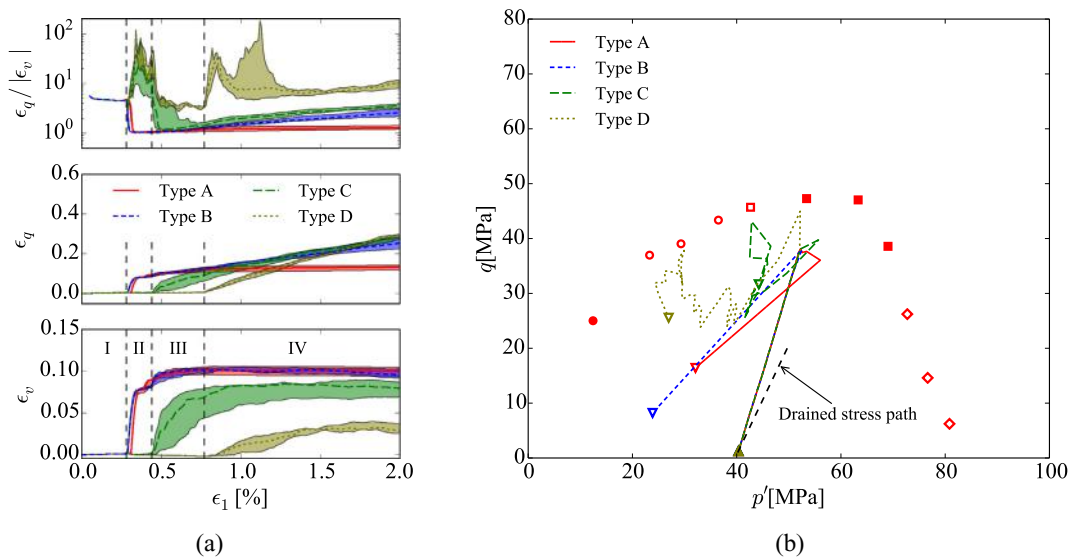


**Fig. 8.** (a) Evolutions of the strain ratio  $\epsilon_q/|\epsilon_v|$ , the deviatoric strain  $\epsilon_q$  and the volumetric strain  $\epsilon_v$  of the selected four types of RVEs in the smooth case under  $\sigma_3 = 40$  MPa. The dashed vertical lines indicate the boundaries between different stages as in Fig. 7a. (b) The effective stress paths of the typical RVEs in each type. See the meanings of different markers in Fig. 6.

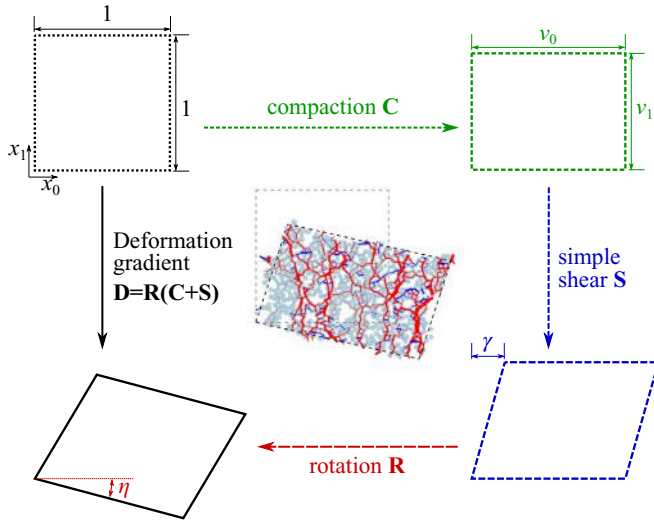


Fig. 9. Illustration of the deformation decomposition. The RVE packing in the center demonstrates a typical RVE (material point) deformation from the original gray square to the final black parallelogram.

in the undrained case due to inhomogeneous build-up of excess pore pressure. Meanwhile,  $\varepsilon_q/|\varepsilon_v|$  proves to be a useful index to characterize the failure modes of the RVEs and to reflect their possible transition under continuous loading.

#### 4.2.4. Microscale deformation features

In the traditional polar decomposition, the deformation gradient ( $\mathbf{D}$ ) is decomposed into a rotation tensor and a symmetric stretch tensor. To quantitatively characterize the deformation features and decouple the volume change and the simple shear part, we decompose the deformation gradient of each RVE with a slight alteration:

$$\mathbf{D} = \mathbf{R}(\mathbf{C} + \mathbf{S}) \quad (4)$$

where  $\mathbf{R} = \begin{bmatrix} \cos \eta & -\sin \eta \\ \sin \eta & \cos \eta \end{bmatrix}$  is the rotation matrix,  $\mathbf{C} = \begin{bmatrix} v_0 & 0 \\ 0 & v_1 \end{bmatrix}$  is the compaction part which may cause volume change and  $\mathbf{S} = \begin{bmatrix} 0 & \gamma \\ 0 & 0 \end{bmatrix}$  is the simple shear part without causing any volume change. The effects of different components are illustrated in Fig. 9. Accordingly, the microscale deformation features of each RVE could be quantitatively described with four scalars: (1) compaction along loading direction (the major principal stress direction)  $(1 - v_1)$ , (2) extension perpendicular to the loading direction (along the minor principal stress direction)  $(v_0 - 1)$ , (3) simple shear deformation ( $\gamma$ ) and (4) rigid-body rotation ( $\eta$ ).

The evolutions of the four decomposed scalar quantities ( $v_1$ ,  $v_0$ ,  $\gamma$  and  $\eta$ ) are plotted against  $\varepsilon_1$  in Fig. 10a. The force chain networks of the selected four types of RVEs at the final state are also plotted in Fig. 10b–e. Type A RVE shows a pure compaction in the loading direction with negligible extension, shear and rotation, which reflects a typical CB feature. The Type B RVE displays a similar behavior with Type A during the CB and transition stages (II and III), but shows a proportionally increased compaction, extension and rotation during the CSB stage (IV). A small shear is noticed at the end of the CSB stage. Type C RVE shows a gradually increased compaction with mild extension, shear and rotation at the transition stage (III). Linear increases in all the four quantities are observed in the CSB stage (IV) for Type C RVE. The Type D RVE exhibits linearly increased compaction, extension, shear and rotation during the CSB stage (IV), which are a typical CSB feature. By comparing the final states of the RVEs, it is concluded that Type A RVE experiences pure compaction in the loading direction, and Type D RVE is subjected to the largest shear and rotation among all

chosen RVEs. Types B and C RVEs are similar to Type D RVE at the end of the CSB stage due to the evolution of the inclined shear band, except that they possess less significant shear and rotation than Type D.

### 4.3. Discussion

#### 4.3.1. Flow patterns and pore pressure distribution

It is worthwhile to examine the fluid flow patterns and the distribution of induced pore pressure during the transition of compaction band. Fig. 11 shows the flow patterns in terms of Darcy flux ( $v_i = -k_{ij}p_{,j}$ ) in conjunction with the fields of incremental volumetric strain ( $\Delta\varepsilon_v = \varepsilon_v^T - \varepsilon_v^{T-1}$ , where  $T$  means the quasi-static loading step) and the distribution of pore pressure at the four selected axial strain levels. The distribution of  $\Delta\varepsilon_v$  serves as a useful indicator for the development of localized failure. In the figure, thicker and longer arrows indicate stronger Darcy flux. Since quasi-static loading condition is considered here, the monitored Darcy flux in our simulations is generally small (in the order of  $10^{-7}$  m/s). So is the difference of pore pressure within the specimen. To highlight the difference, the deviation of pore pressure from its mean value ( $dp = p^I - p$ ) at a loading step is plotted as the right column of Fig. 11. Note that  $dp$  is less than 1 Pa while the mean pore pressure is in the order of 10 MPa.

Stage I shows an almost homogeneous volumetric strain and negligible Darcy flux, which is not shown here. For Stage II, an appreciable flow pattern and variation of  $\Delta\varepsilon_v$  can be observed in Fig. 11a (at  $\varepsilon_1 = 0.32\%$ ). The horizontal extension of CB induces intense in-band compaction (positive  $\Delta\varepsilon_v$ ) and substantial Darcy flux squeezing water out of the band. Note that different colour bars and arrow scale have been used for Fig. 11a for better presentation. Fig. 11c shows the typical flow pattern and  $\Delta\varepsilon_v$  field for Stage III (at  $\varepsilon_1 = 0.72\%$ ). Notably, the magnitudes of both  $\Delta\varepsilon_v$  and Darcy flux are significantly smaller in Stage III than in Stage II. The contour of  $\Delta\varepsilon_v$  clearly demonstrates the concurrent development of the horizontal CB and the inclined band in Stage III. Several clusters of higher  $\Delta\varepsilon_v$  are observed, out of which the Darcy flux is of larger magnitude. The  $\Delta\varepsilon_v$  and Darcy flux become even smaller in Stage IV, as shown in Fig. 11e (at  $\varepsilon_1 = 1.0\%$ ), due to decreasing rate of compaction. The contour of  $\Delta\varepsilon_v$  and the flow pattern show strong evidence of the dominance of the inclined band in Stage IV. The final state at  $\varepsilon_1 = 2.0\%$  as shown in Fig. 11g displays no obvious concentration of  $\Delta\varepsilon_v$  and the Darcy flux in the specimen is nearly negligible.

The distributions of pore pressure at the four selected axial strain levels are plotted as the right column of Fig. 11. Though the difference of pore pressure within the specimen is vanishingly small (less than 1 Pa) compared to the mean pore pressure (in the order of 10 MPa), its distribution offers clear and consistent patterns. Where there is a localized compaction in the specimen, there is a relatively higher pore pressure. Since greater compaction occurs within the horizontal CB in Stage II (see Fig. 11a), a larger in-band deviation of pore pressure  $dp$  is observed in Fig. 11b. As the failure transits from compaction-dominated to shear-dominated with the increase in  $\varepsilon_1$ , the magnitude of  $dp$  decreases gradually. At the final state when  $\varepsilon_1 = 2.0\%$ ,  $dp$  is nearly negligible due to almost homogeneous volumetric strain.

#### 4.3.2. Mesh dependency

The coupled FEM/DEM scheme in this study has been based on a non-regularized FEM formulation which may suffer mesh-dependency. To totally resolve this issue, one needs to resort to various advanced regularization techniques including those based a Cosserat continuum and second gradient theory (Desrues et al., 2019). Nevertheless, using higher-order elements with reasonable fine mesh has been found helpful to mitigate the pathological mesh-dependency of FEM solutions (Guo and Zhao, 2016b). To demonstrate this, two extra cases under the same initial and boundary conditions as the smooth undrained case under  $\sigma_3 = 40$  MPa, but with coarser meshes ( $6 \times 10$  and  $9 \times 15$ ), have been conducted. The solutions from the three different meshes are

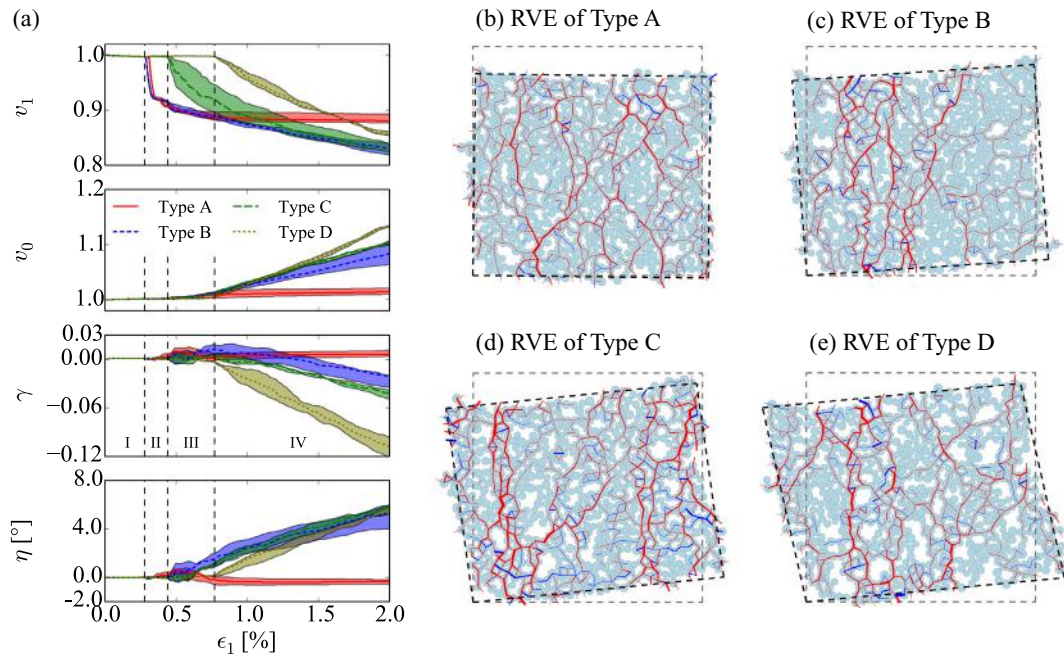


**Fig. 10.** (a) The evolutions of  $v_1$ ,  $v_0$ ,  $\gamma$  and  $\eta$  with the increase in axial strain. The dashed vertical lines indicate the boundaries between different stages as in Fig. 7a. (b–e) The force chain networks of the typical RVEs in each type at the final state. The gray square marks the initial shape of the RVE.

presented in Fig. 12. Fig. 12a displays a comparison of the global responses in terms of  $\sigma_1'$ ,  $N^s$  and  $p$ . Notably, the pre-failure behavior is identical for all three cases, while some mild deviations are observed on the post-peak responses. The  $6 \times 10$  case presents the smallest post-peak  $\sigma_1'$  with the largest  $N^s$ , while the  $12 \times 20$  case displays the largest post-peak  $\sigma_1'$  with the smallest  $N^s$ . The differences become smaller with the increase in  $\epsilon_1$  and the solutions become quite similar in the shear band stage. Fig. 12b–m show the evolution of failure pattern in terms of  $N^l$  with increased  $\epsilon_1$  for the three cases, respectively. Though the predicted band width varies slightly with mesh due to lack of regularization, the evolution of failure pattern appears to be rather consistent in all three cases, initiating from a horizontal compaction band to transit to a shear band of similar dip angle. Consequently, the mesh sensitivity study shows the overall predictions of global responses as well as the occurrence of deformation band patterns (e.g., the orientations) can achieve acceptable consistencies and convergence to render meaningful interpretation of the simulation results.

#### 4.3.3. Transition of compaction fronts

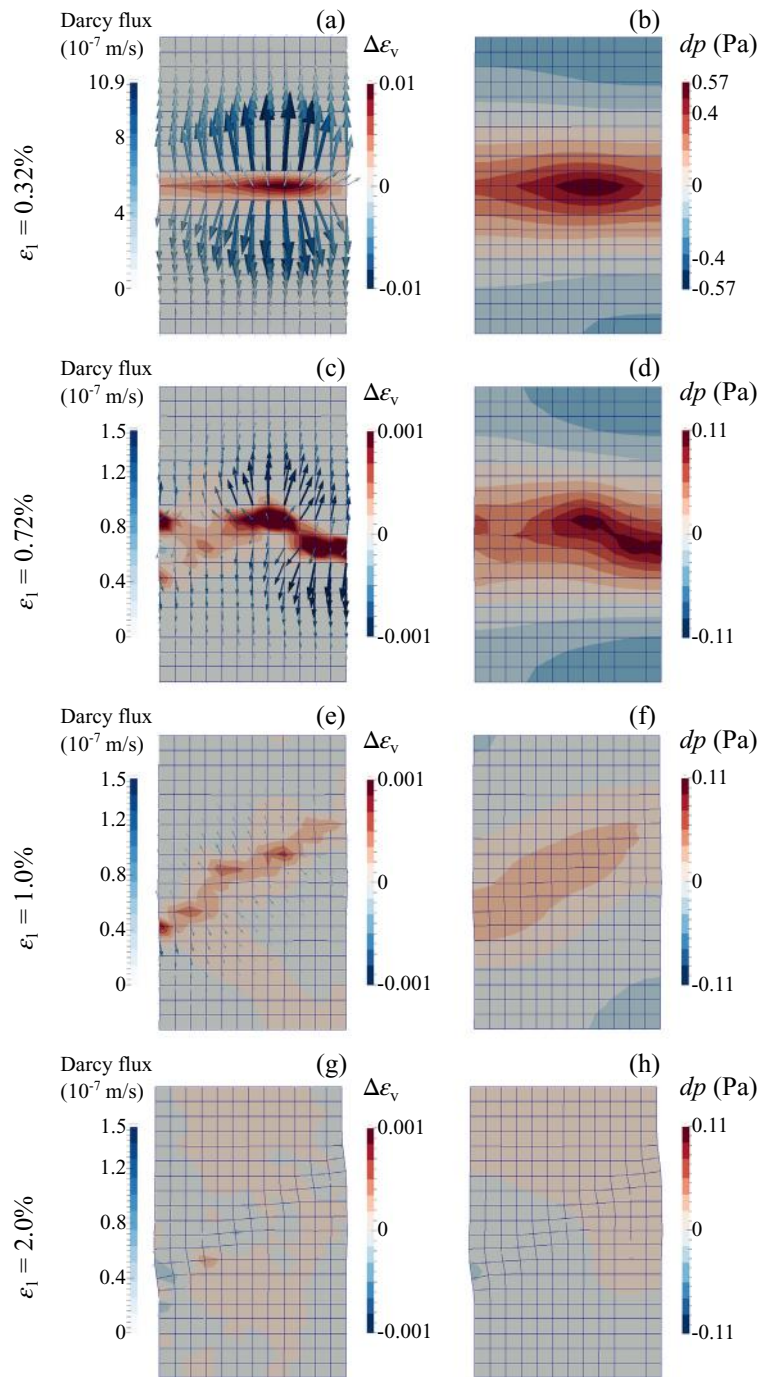
'Compaction fronts', namely localized compaction initiating from the ends of the specimen and propagating towards the center, have been observed in experimental studies on compaction bands possibly due to friction between the specimen and the loading platens (Olsson, 2001). This phenomenon has been reproduced numerically under dry condition with rough loading platens by constraining lateral displacement on the top and the bottom boundaries (Wu et al., 2018a). It is interesting to investigate the evolution of compaction fronts under undrained condition. A homogeneous specimen subjected to undrained shear with rough platens under  $\sigma_3 = 40$  MPa is presented to serve this purpose.

Fig. 13a presents the global response in terms of  $\sigma_1'$ ,  $N^s$  and  $p$ . The specimen is loaded to  $\epsilon_1 = 3.0\%$  until all three global quantities reach steady states. Similar to the smooth case in Section 4.2, the entire process can be divided into (I) elastic stage, (II) CB stage, (III) transition stage and (IV) CSB stage, based on the evolution of the three quantities. As compared to the smooth case, the modulus of the rough case is almost the same (less than 1% difference), while the increasing rate of pore pressure is around 10% larger in the elastic stage. The regions near

the top and bottom boundaries are subjected to a gradually higher effective confinement due to the lateral constraints from the rough loading platens (see detailed stress paths in Fig. 14b). Hence, the stress peak is smaller (63.6 MPa in the rough case and 71.3 MPa in the smooth case) and appears earlier (at  $\epsilon_1 = 0.2\%$  in the rough case and 0.28% in the smooth case, respectively). The initiation of CB stage with a stress drop, a notable increase in  $p$  and a burst of debonding events are similar for the two cases. However, in the rough boundary case, the CB stage lasts longer (from 0.2% to 0.73% in the rough case and from 0.28% to 0.44% in the smooth case) and the CSB stage appears later at a higher axial strain level (1.22% in the rough case and 0.77% in the smooth case). Accordingly, a faster build-up of  $p$  is noted in the rough case. The transition to CSB stage is gentler in the rough case, in contrast to the notable peak in terms of  $N^s$  in the smooth case. It is noteworthy that all the three global quantities approach similar values at the steady states.

Fig. 13b–q present the evolution of band patterns in terms of contours of four local quantities ( $N^l$ ,  $\epsilon_q$ ,  $\epsilon_v$  and  $\theta$ ) at four selected axial strain levels as marked by open circles in Fig. 13a. Fig. 13b–e display a typical band pattern in CB stage with two horizontal compacted regions (CB i and CB ii) near the top and bottom boundaries. In contrast to the planar CB in the smooth case (Fig. 7b–e), the CB in the rough case is somewhat tortuous. An inclined band takes shape from CB i with increased axial strain marking the beginning of transition stage. The inclined band (CSB i) is identified clearly close to the top boundary with a dip angle around  $20^\circ$  in Fig. 13f–i. Similar transition occurs to CB ii at the bottom right corner of the specimen which develops into a pair of conjugate shear bands (see Fig. 13f and j) in late transition stage. CSB ii propagates upwards and becomes dominant later marking the start of CSB stage. It finally cuts through the specimen and intersects with CSB i (see the intersecting bands in Fig. 13j–m). The band pattern at the final stage is shown in Fig. 13n–q. All the bands are noticeable from the contour of  $N^l$ . However, the contours of  $\epsilon_q$  and  $\theta$  are dominated by CSB ii with notable CSB i. On the other hand, CB i and CB ii dominate the contour of  $\epsilon_v$ . The different patterns presented by the four local quantities demonstrate the different nature of the bands.

The local responses of selected RVEs in the major bands in terms of strain evolutions and effective stress paths are presented in Fig. 14 to illustrate the failure mode evolution. CB i and CB ii are regarded as the



**Fig. 11.** Darcy flux (arrows) field, contours of incremental volumetric strain ( $\Delta\epsilon_v$ , left column) and pore pressure deviation from a mean value ( $dp = p^l - p$ , where  $p^l$  is the local pore pressure, right column) at different axial strain levels. Thicker and longer arrows indicate stronger Darcy flux. Note the colour bars and arrow scale for  $\epsilon_1 = 0.32\%$  are different than the other subgraphs.

same and presented as a group. RVEs in CB present typical CB-type strain behavior with a post-failure  $\epsilon_q/|\epsilon_v|$  around 1. The effective stress path of the typical RVE in CB deviates to the right side of the drained stress path due to constraint from the rough boundary and the occurrence of failure at high mean effective stress  $p'$  supports the failure mode as CB. RVEs in CSB i fail during Stage III with a notable peak of  $\epsilon_q/|\epsilon_v|$  and a post-peak value around 4.  $\epsilon_q$  and  $\epsilon_v$  show almost a linear increase in Stage III and stay almost constant in Stage IV. Failure of RVEs in CSB ii starts at the end of Stage III with a gradual increase in  $\epsilon_q/|\epsilon_v|$  to a plateau around 20 in Stage IV. The almost linear increase in  $\epsilon_q$  and  $\epsilon_v$  demonstrates the dominance of CSB ii in Stage IV. The

effective stress paths for CSB i and CSB ii are similar. CSB i is closer to the drained stress path in the elastic stage due to a mild effect of the rough boundary. Their failure at low  $p'$  agrees with their failure mode. CSB ii fails at an even lower  $p'$  in the transitional range between DSB and CSB, which may contribute to the rather mild in-band dilation (see Fig. 13l and Fig. 14a) and the small drop in  $p$  (see Fig. 13a) at the beginning of Stage IV.

#### 4.3.4. Potential implications

Focusing on the interplay between induced pore pressure and the evolution of compaction bands, simulations on undrained biaxial

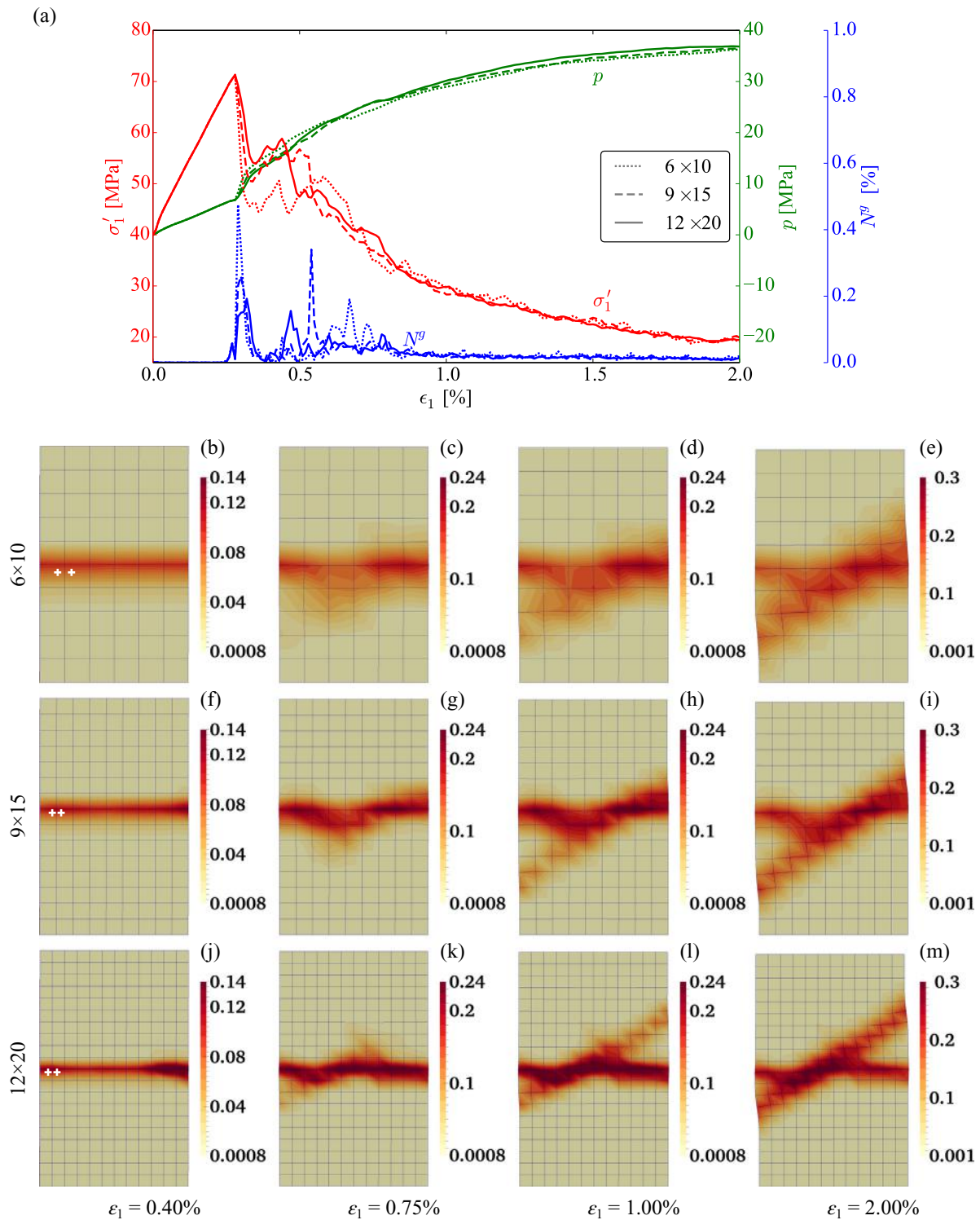
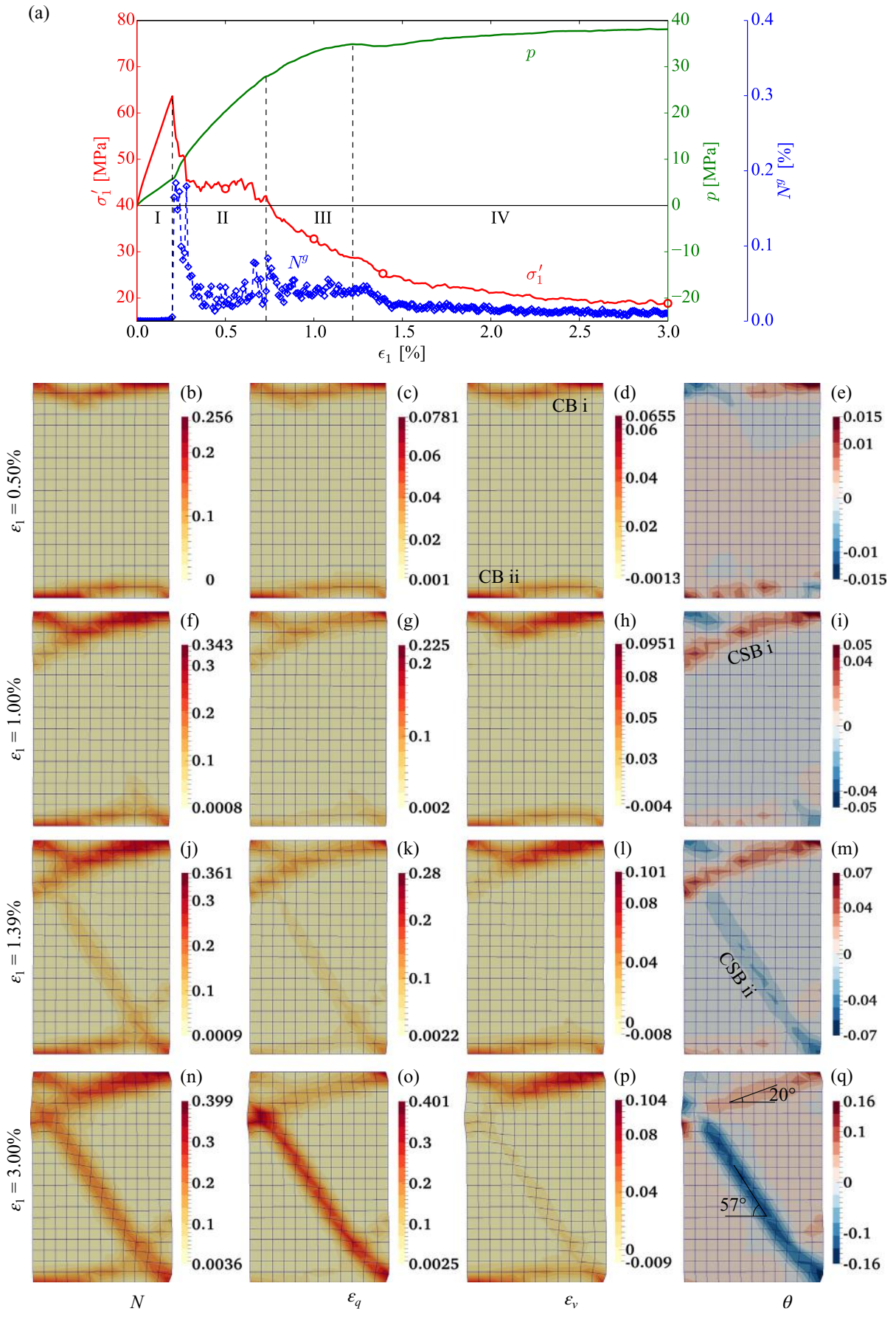


Fig. 12. Mesh-dependency analysis for the hydro-mechanical coupled multiscale modeling. (a) The global responses of the three cases with different mesh density in terms of  $\sigma'_1$ ,  $N^p$  and  $p$ . (b–m) The evolution of failure pattern in terms of  $N^p$  in the three cases with different mesh densities.

compression tests have been conducted as extreme cases with the largest induced pore pressure in contrast to the dry/drained cases with negligible induced pore pressure. Despite a lack of laboratory results for direct comparisons, the evolutions of induced pore pressure and the transition from compaction band to shear band in the undrained simulations may provide important insights into our understanding of compaction band. The induced pore pressure generated during an undrained loading process could be comparable to the total confining

pressure (see the evolutions of  $p$  in Figs. 5a, 7a and 13a) and may influence the initial failure mode and the ensuing evolutions accordingly. Indeed, the experimental measurements of induced pore pressure in undrained triaxial tests (e.g. maximum  $p$  around 16 MPa under  $\sigma_3 = 40$  MPa and maximum  $p$  around 20 MPa under  $\sigma_3 = 50$  MPa) on Fontainebleau sandstone (porosity: 21%) support this possibility, although the applied confining pressure is in the shear band regime (Sulem and Ouffroukh, 2006). The evolution of the band pattern may



(caption on next page)

**Fig. 13.** The transition of compaction fronts in a homogeneous specimen subjected to undrained loading with rough platens under  $\sigma_3 = 40$  MPa. (a) The global responses in terms of  $\sigma_1'$ ,  $N^g$  and  $p$  with increased  $\epsilon_1$ . (b–q) Contours presenting the transition of compaction fronts in terms of  $N^g$ ,  $\epsilon_q$ ,  $\epsilon_v$  and  $\theta$  at four typical axial strain levels (see the four open circles in (a)).

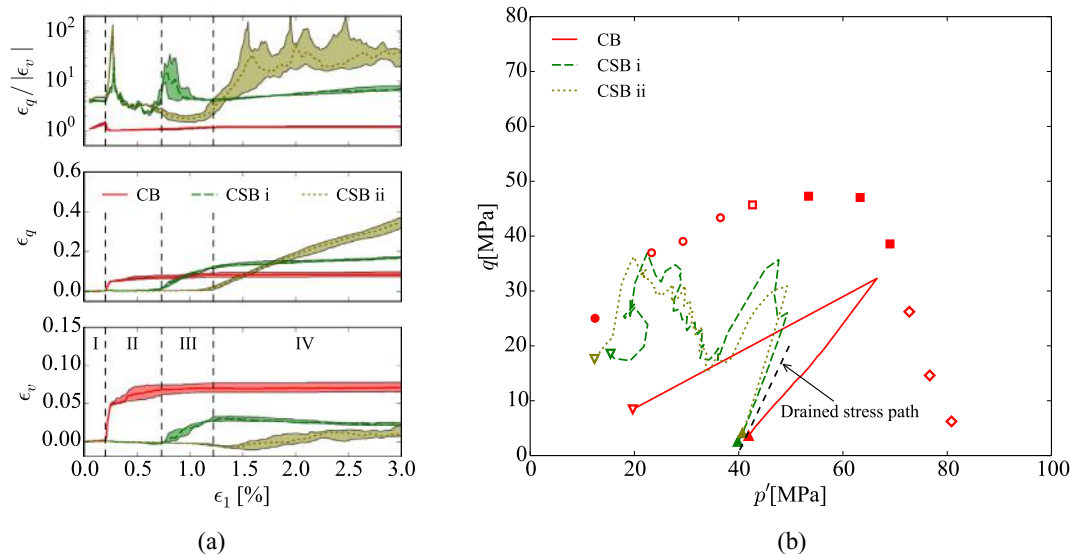


**Fig. 14.** (a) Evolutions of the strain ratio  $\epsilon_q / |\epsilon_v|$ , the deviatoric strain  $\epsilon_q$  and the volumetric strain  $\epsilon_v$ , of the RVEs selected from three major bands in the undrained rough case under  $\sigma_3 = 40$  MPa. (b) The effective stress paths of the typical RVEs in the three major bands. See the meanings of different markers in Fig. 6.

be overlooked if the initial pattern is an inclined band, e.g. the gradual transition from SCB to CSB in the smooth case under  $\sigma_3 = 30$  MPa (see Figs. 5b–i and 6). However, the evolution would be dramatic if the initial pattern is a horizontal CB, e.g. the transition from CB to CSB in Figs. 7b–q and 13b–q.

Laboratory experiments and field investigations revealed that the presence of deformation bands may cause up to several orders of magnitude reduction in permeability as compared to their host rocks, especially when they are presented in clusters (Holcomb and Olsson, 2003; Fossen and Bale, 2007). Those low-permeability deformation bands may act as barriers of pore fluid and form a relatively undrained loading condition. Indeed, Holcomb and Olsson (2003) estimated a compaction-front-induced pore pressure of 0.4 MPa in a cylindrical specimen (5.08 cm by 12.7 cm) subjected to drained loading at a nominal strain rate of  $5$  to  $10 \times 10^{-6} \text{ s}^{-1}$  under  $\sigma_3 = 45$  MPa. The induced pore pressure may become significantly larger (comparable to the confining pressure) and capable of influencing the band pattern, given the effects of rapid loading, larger scale in the field, significant permeability reduction by band clusters and the coexistence of other low permeability structures. The transition from CB to CSB in the undrained simulations under  $\sigma_3 = 40$  MPa generates complex evolving configurations consisting of different types of deformation bands (see Figs. 7 and 13). Interestingly, different types of deformation bands, intersecting or connecting with one another, have been observed in the field outcrops (Deng and Aydin, 2012; Liu et al., 2015). The numerical study presented here complements the prevailing viewpoint that material properties, such as porosity, grain size and grain sorting, control the band pattern (Schultz et al., 2010; Cheung et al., 2012), offering sound numerical evidence and plausible interpretation on the key roles of drainage condition and pore fluid pressure in the study of compaction band.

The study highlights that mean effective stress, an important concept in soil mechanics and poromechanics, plays a controlling role in dictating the inception and evolution of deformation bands in saturated sandstone. Other than advancing our understanding of compaction bands, this finding is also highly relevant to operation and safety for a variety of engineering activities, including borehole drilling and

underground excavations, where altering either in-situ stresses or pore pressure may cause localized deformation, fractures or even failure of relevant geostructures (Sato et al., 2000; Zhao et al., 2014; Wu et al., 2018b). In addition, fluid injection or withdrawal involved in engineering operations (such as hydraulic fracturing) may cause direct variations of pore pressure and hence change of mean effective stress. Evidently, once compactive deformation bands are induced by such changes, the ensuing reduction in permeability may cause highly undesirable adverse consequences to these operation (Holcomb et al., 2007). To name a few, the storage of natural gas or  $\text{CO}_2$  in porous or fracture rocks will cause a build-up in pore pressure (Dieudonné et al., 2015) and promote the formation or transition to shear-dominated failure. On the other hand, the extraction of hydrocarbon or groundwater will lead to a decrease in pore pressure (Motagh et al., 2017; Ochoa-González et al., 2018) and increase the potential to compaction-dominated failure. Therefore, this study identifies this key factor of effective stress based on simulations of drained and undrained biaxial compression tests, in an attempt to provide relevant references to real-world engineering problems.

## 5. Conclusions

A coupled hydro-mechanical multiscale modeling approach has been presented using FEM/DEM hierarchical information-passing scheme to model and understand compaction bands in saturated high-porosity sandstones. Key to the hydro-mechanical coupling is the employment of the popular  $\mathbf{u}$ - $p$  formulation in conjunction with Terzaghi's effective stress principle. The pore pressure  $p$  is treated as a macro variable along with displacement  $\mathbf{u}$ . The effective stress is derived by DEM from the RVE embedded at each Gauss integration point, and is augmented with  $p$  to enter the macro governing equation for a typical solution by FEM. High-porosity RVE has been prepared to represent the typical microstructure of high-porosity sandstones. Multiscale simulations of dry, globally drained and undrained biaxial compression tests have been conducted under different confining pressures to examine the effects of induced pore pressure on the initiation and evolution of compaction bands. Some major findings are summarized below:

1. The effect of induced pore pressure  $p$  on the initial failure mode in high-porosity sandstone is evidently significant. Under undrained conditions where locally pore water may not be able to escape in a timely manner, the build-up of pore pressure can be significant, which may considerably reduce the effective stress and alter the initial failure mode from a compaction band (CB) in the dry or drained condition to a shear-enhanced compaction band (SCB) mode in the undrained case. The further evolution of SCB to compactive shear band (CSB) is also captured in our simulations based on monitoring the deformation features according to strain ratio  $\varepsilon_q/|\varepsilon_v|$ .
2. Under relatively higher confining pressure (e.g., the 40 MPa cases in our study), compaction band may be formed initially, but cannot undergo continuous thickening as observed in a dry case. Instead, the undrained post-failure behavior of the specimen can be characterized by three distinctive stages, namely, the CB stage, the transition stage and the CSB stage, based on analyses of the global responses and features of local quantities. Localized volumetric contraction in sandstone induces relatively higher pore pressure, forming a source for out-of-band flow. The difference in pore pressure and the Darcy flux are largest in the CB stage, but decrease gradually in the ensuing stages.
3. The complex evolution of the failure mode transiting from CB to CSB is analyzed with  $\varepsilon_q/|\varepsilon_v|$  and effective stress path of the in-band RVEs. The analyses demonstrate the capability and robustness of  $\varepsilon_q/|\varepsilon_v|$  in characterizing both the initiation and the development of different failure modes, especially in the presence of pore pressure and pore pressure changes. Distinct microscale deformation features are observed in different band patterns based on the decomposition of deformation gradient extracted from in-band RVEs. The dominance of mean effective stress on the initial failure mode is confirmed with the effective stress paths of the typical in-band RVEs.

The study highlights effective mean (confining) stress as a key controlling macroscopic factor, in addition to porosity, for the occurrence of compaction bands in saturated sandstone. Pore pressure, being a sensitive ambient variable, can change significantly during certain engineering operations, e.g. the extraction of groundwater or hydrocarbon, CO<sub>2</sub> geological sequestration, etc. The change of pore pressure directly leads to change of mean effective stress, and indirectly gives rise to possible pattern changes for deformation bands. The cross-scale analyses provide further confirming evidence to the above conclusion. Notably, however, all studied cases in this paper have assumed two attributing micro-mechanisms: pore collapse and inter-granular debonding, without account for particle crushing (as the same in Wu et al., 2018a). The simplification highlights the possibility of our assumed high-porosity structure to trigger compaction bands, but by no means it denies the importance of grain crushing. Indeed, the rather brittle stress drop at failure might be a possible consequence of neglecting grain crushing in our modeling. Simulating grain crushing is challenging and may have to involve many unrealistic assumptions. Nevertheless, the incorporation of grain crushing is our next step on multiscale modeling of sandstone. Furthermore, we have adopted an isotropic permeability based on the empirical Kozeny–Carman equation in this study. This may lead to underestimated permeability reduction caused by compaction bands. In reality, grain crushing and increased tortuosity may both cause clogging effects for fluid flow. An anisotropic permeability considering the evolution of particle size and tortuosity will definitely improve the predictive capability of the current model and facilitate the understanding of the underlying hydromechanical interaction mechanisms, which will be considered in the future.

## Acknowledgments

The study has been financially supported by the National Natural Science Foundation of China under project 51679207 and the Research

Grants Council of Hong Kong through GRF project 16210017 and CRF CC6012-15G. NG has been financially supported by the National Natural Science Foundation of China under project 51809229. The software code used for modeling and generating the data in this study is based on the open-source parallel hierarchical multiscale modeling code FEM×DEM accessible via Yade (<https://yade-dem.org/doc/FEMxDEM.html>). All figures were generated by the open-source data analysis toolkit (Python with the NumPy/SciPy and matplotlib packages, Paraview and Inkscape).

## References

- Andrade, J.E., Borja, R.I., 2007. Modeling deformation banding in dense and loose fluid-saturated sands. *Finite Elem. Anal. Des.* 43, 361–383. <https://doi.org/10.1016/j.finel.2006.11.012>.
- Argilaga, A., Desrues, J., Pont, S.D., Combe, G., Caillerie, D., 2018. FEMDEM multiscale modeling: model performance enhancement from Newton strategy to element loop parallelization. *Int. J. Numer. Methods Eng.* 114, 47–65. <https://doi.org/10.1002/nme.5732>.
- Aydin, A., Ahmadov, R., 2009. Bed-parallel compaction bands in aeolian sandstone: their identification, characterization and implications. *Tectonophysics* 479, 277–284. <https://doi.org/10.1016/j.tecto.2009.08.033>.
- Baud, P., Klein, E., Wong, T.F., 2004. Compaction localization in porous sandstones: spatial evolution of damage and acoustic emission activity. *J. Struct. Geol.* 26, 603–624. <https://doi.org/10.1016/j.jsg.2003.09.002>.
- Baud, P., Meredith, P., Townend, E., 2012. Permeability evolution during triaxial compaction of an anisotropic porous sandstone. *J. Geophys. Res.* 117, B05203. <https://doi.org/10.1029/2012JB009176>.
- Baud, P., Reuschlé, T., Ji, Y., Cheung, C.S.N., Wong, T.F., 2015. Mechanical compaction and strain localization in Bleurswiller sandstone. *J. Geophys. Res. Solid Earth* 120, 6501–6522. <https://doi.org/10.1002/2015JB012192>.
- Biot, M.A., 1941. General theory of three-dimensional consolidation. *J. Appl. Phys.* 12, 155–164. <https://doi.org/10.1063/1.1712886>.
- Budarapu, P.R., Gracie, R., Yang, S.W., Zhuang, X., Rabczuk, T., 2014. Efficient coarse graining in multiscale modeling of fracture. *Theor. Appl. Fract. Mech.* 69, 126–143. <https://doi.org/10.1016/j.tafmec.2013.12.004>.
- Chang, C., Haimson, B.C., 2007. Effect of fluid pressure on rock compressive failure in a nearly impermeable crystalline rock: implication on mechanism of borehole break-outs. *Eng. Geol.* 89, 230–242. <https://doi.org/10.1016/j.enggeo.2006.10.006>.
- Charalampidou, E.M., Hall, S.A., Stanchits, S., Lewis, H., Viggiani, G., 2011. Characterization of shear and compaction bands in a porous sandstone deformed under triaxial compression. *Tectonophysics* 503, 8–17. <https://doi.org/10.1016/j.tecto.2010.09.032>.
- Charalampidou, E.M., Hall, S.A., Stanchits, S., Viggiani, G., Lewis, H., 2014. Shear-enhanced compaction band identification at the laboratory scale using acoustic and full-field methods. *Int. J. Rock Mech. Min. Sci.* 67, 240–252. <https://doi.org/10.1016/j.ijrmm.2013.05.006>.
- Cheung, C.S.N., Baud, P., Wong, T.F., 2012. Effect of grain size distribution on the development of compaction localization in porous sandstone. *Geophys. Res. Lett.* 39, 6–10. <https://doi.org/10.1029/2012GL053739>.
- Das, A., Buscarnera, G., 2014. Simulation of localized compaction in high-porosity calcarenite subjected to boundary constraints. *Int. J. Rock Mech. Min. Sci.* 71, 91–104. <https://doi.org/10.1016/j.ijrmm.2014.07.004>.
- Deng, S., Aydin, A., 2012. Distribution of compaction bands in 3D in an aeolian sandstone: the role of cross-bed orientation. *Tectonophysics* 574–575, 204–218. <https://doi.org/10.1016/j.tecto.2012.08.037>.
- Desrues, J., Argilaga, A., Caillerie, D., Combe, G., Nguyen, T.K., Richefeu, V., Pont, S.D., 2019. From discrete to continuum modelling of boundary value problems in geomechanics: an integrated FEM-DEM approach. *Int. J. Numer. Anal. Methods Geomech.* 43, 919–955. <https://doi.org/10.1002/nag.2914>.
- Dieudonné, A.C., Cerfontaine, B., Collin, F., Charlier, R., 2015. Hydromechanical modelling of shaft sealing for CO<sub>2</sub> storage. *Eng. Geol.* 193, 97–105. <https://doi.org/10.1016/j.enggeo.2015.04.016>.
- Fortin, J., Stanchits, S., Dresen, G., Guéguen, Y., 2006. Acoustic emission and velocities associated with the formation of compaction bands in sandstone. *J. Geophys. Res.* 111, B10203. <https://doi.org/10.1029/2005JB003854>.
- Fossen, H., Bale, A., 2007. Deformation bands and their influence on fluid flow. *AAPG Bull.* 91, 1685–1700. <https://doi.org/10.1306/07300706146>.
- Fossen, H., Soliva, R., Ballas, G., Trzaskos, B., Cavalcante, C., Schultz, R.A., 2017. A review of deformation bands in reservoir sandstones: geometries, mechanisms and distribution. *Geol. Soc. Lond., Spec. Publ.* 459, 9–33. <https://doi.org/10.1144/SP459.4>.
- Gomez, C.T., Dvorkin, J., Vanorio, T., 2010. Laboratory measurements of porosity, permeability, resistivity, and velocity on Fontainebleau sandstones. *Geophysics* 75, E191. <https://doi.org/10.1190/1.3493633>.
- Guo, N., Zhao, J., 2014. A coupled FEM/DEM approach for hierarchical multiscale modelling of granular media. *Int. J. Numer. Methods Eng.* 99, 789–818. <https://doi.org/10.1002/nme.4702>.
- Guo, N., Zhao, J., 2016a. 3D multiscale modeling of strain localization in granular media. *Comput. Geotech.* 80, 360–372. <https://doi.org/10.1016/j.compgeo.2016.01.020>.
- Guo, N., Zhao, J., 2016b. Multiscale insights into classical geomechanics problems. *Int. J. Numer. Anal. Methods Geomech.* 40, 367–390. <https://doi.org/10.1002/nag.2406>.

- Guo, N., Zhao, J., 2016c. Parallel hierarchical multiscale modelling of hydro-mechanical problems for saturated granular soils. *Comput. Methods Appl. Mech. Eng.* 305, 768–785. <https://doi.org/10.1016/j.cma.2016.03.004>.
- Haimson, B.C., Kovacich, J., 2003. Borehole instability in high-porosity Berea sandstone and factors affecting dimensions and shape of fracture-like breakouts. *Eng. Geol.* 69, 219–231. [https://doi.org/10.1016/S0013-7952\(02\)00283-1](https://doi.org/10.1016/S0013-7952(02)00283-1).
- Haimson, B.C., Lee, H., 2004. Borehole breakouts and compaction bands in two high-porosity sandstones. *Int. J. Rock Mech. Min. Sci.* 41, 287–301. <https://doi.org/10.1016/j.ijrmms.2003.09.001>.
- Hall, S.A., 2013. Characterization of fluid flow in a shear band in porous rock using neutron radiography. *Geophys. Res. Lett.* 40, 2613–2618. <https://doi.org/10.1002/grl.50528>.
- Hamdia, K.M., Silani, M., Zhuang, X., He, P., Rabczuk, T., 2017. Stochastic analysis of the fracture toughness of polymeric nanoparticle composites using polynomial chaos expansions. *Int. J. Fract.* 206, 215–227. <https://doi.org/10.1007/s10704-017-0210-6>.
- Holcomb, D.J., Olsson, W.A., 2003. Compaction localization and fluid flow. *J. Geophys. Res.* 108, 2290. <https://doi.org/10.1029/2001JB000813>.
- Holcomb, D., Rudnicki, J.W., Issen, K.A., Sternlof, K., 2007. Compaction localization in the Earth and the laboratory: state of the research and research directions. *Acta Geotech.* 2, 1–15. <https://doi.org/10.1007/s11440-007-0027-y>.
- Issen, K.A., Rudnicki, J.W., 2000. Conditions for compaction bands in porous rock. *J. Geophys. Res.* 105, 21529–21536. <https://doi.org/10.1029/2000JB900185>.
- Katsman, R., Aharonov, E., Scher, H., 2006. A numerical study on localized volume reduction in elastic media: some insights on the mechanics of anticracks. *J. Geophys. Res.* 111, B03204. <https://doi.org/10.1029/2004JB003607>.
- Kimura, S., Kaneko, H., Noda, S., Ito, T., Minagawa, H., 2018. Shear-induced permeability reduction and shear-zone development of sand under high vertical stress. *Eng. Geol.* 238, 86–98. <https://doi.org/10.1016/j.enggeo.2018.02.018>.
- Liu, C., Pollard, D.D., Deng, S., Aydin, A., 2015. Mechanism of formation of wiggly compaction bands in porous sandstone: 1. Observations and conceptual model. *J. Geophys. Res.* Solid Earth 120, 8138–8152. <https://doi.org/10.1002/2015JB012372>.
- Mollema, P.N., Antonellini, M.A., 1996. Compaction bands: a structural analog for anti-mode I cracks in aeolian sandstone. *Tectonophysics* 267, 209–228. [https://doi.org/10.1016/S0040-1951\(96\)00098-4](https://doi.org/10.1016/S0040-1951(96)00098-4).
- Motagh, M., Shamshiri, R., Haghshenas Haghghi, M., Wetzel, H.U., Akbari, B., Nahavandchi, H., Roessner, S., Arabi, S., 2017. Quantifying groundwater exploitation induced subsidence in the Rafsanjan plain, southeastern Iran, using InSAR time-series and in situ measurements. *Eng. Geol.* 218, 134–151. <https://doi.org/10.1016/j.enggeo.2017.01.011>.
- Ochoa-González, G.H., Carreón-Freyre, D., Franceschini, A., Cerca, M., Teatini, P., 2018. Overexploitation of groundwater resources in the faulted basin of Querétaro, Mexico: a 3D deformation and stress analysis. *Eng. Geol.* 245, 192–206. <https://doi.org/10.1016/j.enggeo.2018.08.014>.
- Olsson, W.A., 2001. Quasistatic propagation of compaction fronts in porous rock. *Mech. Mater.* 33, 659–668. [https://doi.org/10.1016/S0167-6636\(01\)00078-3](https://doi.org/10.1016/S0167-6636(01)00078-3).
- Ougier-Simonin, A., Zhu, W., 2013. Effects of pore fluid pressure on slip behaviors: an experimental study. *Geophys. Res. Lett.* 40, 2619–2624. <https://doi.org/10.1002/grl.50543>.
- Pons, A., David, C., Fortin, J., Stanchits, S., Menéndez, B., Mengus, J.M., 2011. X-ray imaging of water motion during capillary imbibition: a study on how compaction bands impact fluid flow in Bentheim sandstone. *J. Geophys. Res.* 116, B03205. <https://doi.org/10.1029/2010JB007973>.
- Sato, T., Kikuchi, T., Sugihara, K., 2000. In-situ experiments on an excavation disturbed zone induced by mechanical excavation in Neogene sedimentary rock at Tono mine, Central Japan. *Eng. Geol.* 56, 97–108. [https://doi.org/10.1016/S0013-7952\(99\)00136-2](https://doi.org/10.1016/S0013-7952(99)00136-2).
- Schultz, R.A., Okubo, C.H., Fossen, H., 2010. Porosity and grain size controls on compaction band formation in Jurassic Navajo Sandstone. *Geophys. Res. Lett.* 37, 1–5. <https://doi.org/10.1029/2010GL044909>.
- Shahin, G., Desrués, J., Pont, S.D., Combe, G., Argilaga, A., 2016. A study of the influence of REV variability in double-scale FEM DEM analysis. *Int. J. Numer. Methods Eng.* 107, 882–900. <https://doi.org/10.1002/nme.5202>.
- Soliva, R., Schultz, R.A., Ballas, G., Taboada, A., Wibberley, C., Sallet, E., Benedetto, A., 2013. A model of strain localization in porous sandstone as a function of tectonic setting, burial and material properties; new insight from Provence (southern France). *J. Struct. Geol.* 49, 50–63. <https://doi.org/10.1016/j.jsg.2012.11.011>.
- Sulem, J., Ouffroukh, H., 2006. Shear banding in drained and undrained triaxial tests on a saturated sandstone: porosity and permeability evolution. *Int. J. Rock Mech. Min. Sci.* 43, 292–310. <https://doi.org/10.1016/j.ijrmms.2005.07.001>.
- Sun, W., Andrade, J.E., Rudnicki, J.W., Eichhubl, P., 2011. Connecting microstructural attributes and permeability from 3D tomographic images of in situ shear-enhanced compaction bands using multiscale computations. *Geophys. Res. Lett.* 38, L10301. <https://doi.org/10.1029/2011GL047683>.
- Sun, W.C., Kuhn, M.R., Rudnicki, J.W., 2013. A multiscale DEM-LBM analysis on permeability evolutions inside a dilatant shear band. *Acta Geotech.* 8, 465–480. <https://doi.org/10.1007/s11440-013-0210-2>.
- Talebi, H., Silani, M., Bordas, S.P.A., Kerfriden, P., Rabczuk, T., 2014. A computational library for multiscale modeling of material failure. *Comput. Mech.* 53, 1047–1071. <https://doi.org/10.1007/s00466-013-0948-2>.
- Tembe, S., Baud, P., Wong, T.F., 2008. Stress conditions for the propagation of discrete compaction bands in porous sandstone. *J. Geophys. Res.* 113, B09409. <https://doi.org/10.1029/2007JB005439>.
- Terzaghi, K., 1943. *Theoretical Soil Mechanics*. John Wiley & Sons, Inc., Hoboken, NJ, USA. <https://doi.org/10.1002/9780470172766>.
- Wasantha, P.L.P., Ranjith, P.G., 2014. Water-weakening behavior of Hawkesbury sandstone in brittle regime. *Eng. Geol.* 178, 91–101. <https://doi.org/10.1016/j.enggeo.2014.05.015>.
- Wasantha, P.L.P., Ranjith, P.G., Viete, D.R., 2016. Hydro-mechanical behavior of sandstone with interconnected joints under undrained conditions. *Eng. Geol.* 207, 66–77. <https://doi.org/10.1016/j.enggeo.2016.04.004>.
- Wu, H., Guo, N., Zhao, J., 2017. Borehole instabilities in granular rocks revisited: a multiscale perspective. In: Papamichos, E., Papanastasiou, P., Pasternak, E., Dyskin, A. (Eds.), *Bifurcation and Degradation of Geomaterials with Engineering Applications*. Springer, Cham, pp. 433–439. [https://doi.org/10.1007/978-3-319-56397-8\\_54](https://doi.org/10.1007/978-3-319-56397-8_54).
- Wu, H., Guo, N., Zhao, J., 2018a. Multiscale modeling and analysis of compaction bands in high-porosity sandstones. *Acta Geotech.* 13, 575–599. <https://doi.org/10.1007/s11440-017-0560-2>.
- Wu, H., Zhao, J., Guo, N., 2018b. Multiscale insights into borehole instabilities in high-porosity sandstones. *J. Geophys. Res.* Solid Earth 123, 3450–3473. <https://doi.org/10.1029/2017JB015366>.
- Zhang, Q., Li, X., Bai, B., Hu, H., 2019. The shear behavior of sandstone joints under different fluid and temperature conditions. *Eng. Geol.* 257, 105143. <https://doi.org/10.1016/j.enggeo.2019.05.020>.
- Zhao, J., Shan, T., 2013. Coupled CFD–DEM simulation of fluid–particle interaction in geomaterials. *Powder Technol.* 239, 248–258. <https://doi.org/10.1016/j.powtec.2013.02.003>.
- Zhao, K., Janutolo, M., Barla, G., Chen, G., 2014. 3D simulation of TBM excavation in brittle rock associated with fault zones: the Brenner Exploratory Tunnel case. *Eng. Geol.* 181, 93–111. <https://doi.org/10.1016/j.enggeo.2014.07.002>.
- Zienkiewicz, O.C., Chan, A.H.C., 1989. Coupled problems and their numerical solution. In: Doltsinis, I.S. (Ed.), *Advances in Computational Nonlinear Mechanics*. Springer Vienna, Vienna, pp. 139–176. [https://doi.org/10.1007/978-3-7091-2828-2\\_4](https://doi.org/10.1007/978-3-7091-2828-2_4).